

**Time- and frequency-dependent model of time-resolved coherent anti-Stokes Raman scattering (CARS) with a picosecond-duration probe pulse**

Hans U. Stauffer, Joseph D. Miller, Mikhail N. Slipchenko, Terrence R. Meyer, Benjamin D. Prince, Sukesh Roy, and James R. Gord

Citation: [The Journal of Chemical Physics](#) **140**, 024316 (2014); doi: 10.1063/1.4860475

View online: <http://dx.doi.org/10.1063/1.4860475>

View Table of Contents: <http://scitation.aip.org/content/aip/journal/jcp/140/2?ver=pdfcov>

Published by the [AIP Publishing](#)

---



## Re-register for Table of Content Alerts

Create a profile.



Sign up today!



# Time- and frequency-dependent model of time-resolved coherent anti-Stokes Raman scattering (CARS) with a picosecond-duration probe pulse

Hans U. Stauffer,<sup>1,a)</sup> Joseph D. Miller,<sup>2,3</sup> Mikhail N. Slipchenko,<sup>1</sup> Terrence R. Meyer,<sup>3</sup> Benjamin D. Prince,<sup>4</sup> Sukesh Roy,<sup>1</sup> and James R. Gord<sup>2</sup>

<sup>1</sup>*Spectral Energies, LLC, 5100 Springfield St., Suite 301, Dayton, Ohio 45431, USA*

<sup>2</sup>*Air Force Research Laboratory, Aerospace Systems Directorate, Wright-Patterson AFB, Ohio 45433, USA*

<sup>3</sup>*Department of Mechanical Engineering, Iowa State University, Ames, Iowa 50011, USA*

<sup>4</sup>*Air Force Research Laboratory, Space Vehicles Directorate, Kirtland AFB, New Mexico 87117, USA*

(Received 12 September 2013; accepted 16 December 2013; published online 14 January 2014)

The hybrid femtosecond/picosecond coherent anti-Stokes Raman scattering (fs/ps CARS) technique presents a promising alternative to either fs time-resolved or ps frequency-resolved CARS in both gas-phase thermometry and condensed-phase excited-state dynamics applications. A theoretical description of time-dependent CARS is used to examine this recently developed probe technique, and quantitative comparisons of the full time–frequency evolution show excellent accuracy in predicting the experimental vibrational CARS spectra obtained for two model systems. The interrelated time- and frequency-domain spectral signatures of gas-phase species produced by hybrid fs/ps CARS are explored with a focus on gas-phase N<sub>2</sub> vibrational CARS, which is commonly used as a thermometric diagnostic of combusting flows. In particular, we discuss the merits of the simple top-hat spectral filter typically used to generate the ps-duration hybrid fs/ps CARS probe pulse, including strong discrimination against non-resonant background that often contaminates CARS signal. It is further demonstrated, via comparison with vibrational CARS results on a time-evolving solvated organic chromophore, that this top-hat probe-pulse configuration can provide improved spectral resolution, although the degree of improvement depends on the dephasing timescales of the observed molecular modes and the duration and timing of the narrowband final pulse. Additionally, we discuss the virtues of a frequency-domain Lorentzian probe-pulse lineshape and its potential for improving the hybrid fs/ps CARS technique as a diagnostic in high-pressure gas-phase thermometry applications. © 2014 AIP Publishing LLC. [<http://dx.doi.org/10.1063/1.4860475>]

## I. INTRODUCTION

Hybrid femtosecond/picosecond coherent anti-Stokes Raman scattering (fs/ps CARS)<sup>1–4</sup> is a powerful optical detection technique that has proven particularly beneficial as a thermometric diagnostic tool in combustion environments.<sup>5–12</sup> This probe technique has been developed as a variant of fs time-resolved CARS (tr-CARS),<sup>13–25</sup> the history of which has been described thoroughly in recent reviews.<sup>26,27</sup> Hybrid fs/ps CARS utilizes the same four-wave-mixing excitation scheme as does fs tr-CARS; however, the use of a time-delayed, narrowband, ps-duration probe pulse—rather than a broadband, fs-duration probe pulse—allows direct frequency-domain detection of Raman-active molecular states.<sup>1,3</sup> As such, this detection approach retains the chemical specificity associated with Raman spectroscopy,<sup>1,3</sup> with excellent detection sensitivity.<sup>4</sup> The spectral resolution of hybrid fs/ps CARS signal, furthermore, allows single-shot thermometry and multi-species measurements in reacting flows at repetition rates in the kHz range,<sup>5,11,12,28</sup> and several hybrid fs/ps CARS schemes have been used to probe gas-phase vibrational<sup>5,6</sup> and

rotational<sup>7–12,29–31</sup> CARS spectra. In addition to the multiplex nature of this newer probe technique, hybrid fs/ps CARS also provides the additional feature that Raman-active rotational/vibrational frequencies can be directly recovered;<sup>1</sup> they do not need to be deduced from time-dependent coherent oscillations observed in the spectrally dispersed CARS signal beam, as is the case in fs tr-CARS.<sup>20,32,33</sup> We note further that many of the advantages typically ascribed to fs tr-CARS<sup>26,34</sup> are retained in hybrid fs/ps CARS.<sup>1,3</sup> In particular, strong, undesirable contributions from non-resonant (NR) CARS (often referred to as electronic contributions) that generally complicate frequency-domain, nanosecond (ns), and ps tr-CARS probes<sup>35</sup> can be discriminated against in both fs tr-CARS and hybrid fs/ps CARS by precisely varying the timing between the three input CARS pulses. Moreover, this multiplexing allows the use of the hybrid fs/ps CARS technique as an efficient probe following molecular excitation via an initial ultrafast pulse. Thus, hybrid fs/ps CARS can be used to probe the evolution of non-equilibrium excited states in much the same way that fs tr-CARS and the related time-resolved degenerate four wave mixing (DFWM) have been used in these applications (often referred to as pump-CARS and pump-DFWM, respectively).<sup>36–46</sup> For example, this probe technique has been used to observe the excited-state evolution of coumarin 153

<sup>a)</sup> Author to whom correspondence should be addressed. Electronic mail: [hans.stauffer@gmail.com](mailto:hans.stauffer@gmail.com)

with vibrational resolution to probe the timescales associated with hydrogen-bond cleavage and reformation in protic solvents.<sup>47</sup>

An important distinguishing feature of hybrid fs/ps CARS is the interrelationship between the observed state-resolved frequency-domain signal and the time delay of the final ps-duration probe pulse. This interrelationship exists because the hybrid fs/ps CARS probe-pulse frequency-domain bandwidths are specifically chosen to be spectrally narrow enough to resolve molecular transitions of interest. By virtue of the time–frequency uncertainty principle, the resultant probe-pulse duration is typically of the order of 1–10 ps, which still provides sufficient temporal resolution to discriminate against NR contaminating signal. The interdependence between the time- and frequency-domain signals is particularly significant in cases where molecular dephasing timescales are comparable to or longer than the probe-pulse duration; under these conditions, both the transition frequencies and lineshapes of the observed CARS signal can exhibit a notable temporal dependence.<sup>5,10</sup> As such, direct comparison to computational simulations is imperative for quantitative interpretation of the experimental results. The hybrid fs/ps CARS technique has been described previously via experimental comparison with traditional fs tr-CARS,<sup>1,2</sup> and some computational simulations of tr-CARS were used in prior work<sup>1,3</sup> that emphasize the similarities and differences between these two related optical techniques. This initial work focused primarily on the advantages of hybrid fs/ps CARS as a simultaneously vibrationally resolved and time-resolved probe, however, without providing a thorough treatment of the theoretical aspects of the hybrid fs/ps CARS probe. The general benefits associated with a time-delayed probe have also been explored theoretically,<sup>4,48</sup> although the emphasis of that work is on a probe pulse with a Gaussian temporal profile rather than with temporal profiles matching those used experimentally. More recent applications of the hybrid fs/ps CARS technique to gas-phase thermometry<sup>5–12,31</sup> have generally highlighted the agreement between experiment and simulation at single probe delays with an emphasis on the corresponding thermometric accuracy and precision afforded by reasonable simulation. The emphasis of this current work is on providing a thorough theoretical description of the hybrid fs/ps CARS probe technique, accompanied by full simulations of the time evolution of experimental spectra and expected lineshapes and intensities, in order to explore further the inherent advantages and limitations of this probe technique.

The discussion below explores the interrelated frequency- and time-dependent signals that result from application of the hybrid fs/ps CARS approach. In order to provide a thorough experimental validation of the predictions resulting from a theoretical time-dependent CARS formulation, a brief description is given of two different experimental systems, including gas-phase N<sub>2</sub> and a solvated  $\pi$ -conjugated organic molecular species (*trans*-4-dimethylamino-4'-nitrostilbene [DANS] dissolved in acetonitrile [ACN]). This allows exploration of the effects of probe delay for two cases where the molecular decay timescales are, respectively, much longer than and comparable to the duration of the

hybrid fs/ps CARS probe pulse. A discussion of experimental arrangements is followed by a general description of the time- and frequency-dependent theoretical framework that can be applied to describe the signals expected in a vast array of sub-ns tr-CARS experiments, including fs tr-CARS, ps-CARS, and hybrid fs/ps CARS. Because this theoretical CARS description is applicable to optical configurations involving a variety of probe-pulse spectral shapes and temporal profiles, the expected signals arising from several probe-pulse configurations are explored, with an emphasis, when possible, on the derivation of analytical expressions that illuminate the expected lineshapes and temporal dependence under each of these conditions. In particular, the two limiting cases involving a short, broadband probe pulse (Appendix B); and a long, frequency-narrow probe pulse (Appendix C) are discussed to emphasize the robustness of this time-domain theoretical model to cases where the molecular spectral signatures are exclusively observed in the time and frequency domains, respectively. We subsequently explore the predicted time- and frequency-dependent signals arising from the two probe-pulse shapes that are commonly used in hybrid fs/ps CARS experiments; these include (a) a top-hat (i.e., square pulse) frequency-domain amplitude filter; and (b) a Lorentzian spectral filter. This approach provides a predictive description of the lineshapes and frequencies observed using the hybrid fs/ps CARS technique, both in the presence and absence of overlapping resonant and NR signal.

## II. EXPERIMENTAL SETUP

### A. Gas phase experiments: N<sub>2</sub> vibrational CARS

The details of the experimental hybrid fs/ps CARS approach used to obtain the gas-phase vibrational CARS data described below have been presented previously,<sup>5</sup> and only a brief description will be presented here. The 790-nm output of a regeneratively amplified Ti:sapphire laser (pulse duration  $\sim 100$  fs) is divided into Stokes and probe beams. A third portion of this fundamental output is used to pump an optical parametric amplifier (OPA), which produces the broadband (full-width-at-half-maximum [FWHM] bandwidth of  $\Delta\omega \approx 150$  cm<sup>-1</sup>) pump beam centered near 668 nm; this wavelength is selected to provide access to the  $Q$ -branch transition region of the  $\Delta v = 1$  vibrational spectrum of nitrogen gas near 2300 cm<sup>-1</sup>. The probe beam is generated using a grating-based folded 4- $f$  pulse shaper<sup>49</sup> containing an adjustable slit at its focal plane to allow simple frequency-domain top-hat amplitude shaping of the probe pulse. The three CARS beams interact with the sample in a folded-BOXCARS arrangement; in the experiments described here, the sample is the N<sub>2</sub> gas present within a laminar non-premixed H<sub>2</sub>–air flame stabilized over a flat-flame Hencken calibration burner at an adiabatic flame temperature of 2370 K.<sup>50</sup> Temporal delay of the probe pulse with respect to the time-overlapped pump and Stokes pulses is facilitated using a computer-controlled translation stage. The outgoing CARS signal beam produced by the interaction of the three input beams with the sample is spatially filtered and spectrally resolved using a 1.26-m spectrometer equipped with a 600-line/mm

grating and an electron-multiplying charge-coupled-device (EMCCD) detector.

## B. Condensed phase experiments: DANS vibrational CARS

In order to emphasize the lineshape dependence of the hybrid fs/ps CARS signal on the delay of the shaped probe pulse, it is important to explore an experimental system in which the molecular decay timescales are comparable to or faster than the duration of the optical probe pulse. Therefore, some of the experimental results discussed here involve hybrid fs/ps CARS experiments on DANS (Aldrich, 97%) dissolved in ACN (Fisher, HPLC grade) to  $\sim 1$  mM concentration. The sample solution is placed in the 220- $\mu\text{m}$  gap between two fused silica windows in a rotating cell that allows complete sample refreshment between laser shots. The optical system used in these experiments has been discussed in detail previously,<sup>1</sup> and differs from the system used in the gas-phase experiments primarily in the use of different wavelengths for the pump (510 nm;  $\Delta\omega \approx 250$   $\text{cm}^{-1}$ ) and Stokes (550 nm;  $\Delta\omega \approx 250$   $\text{cm}^{-1}$ ) pulses, selected to allow access to vibrational transitions in the 1000–1700  $\text{cm}^{-1}$  “fingerprint” spectral range, and amplitude-shaped probe (795 nm; square pulse width of 15  $\text{cm}^{-1}$ ) pulse. Furthermore, since the discussed experiments are carried out following electronic excitation of DANS, an excitation pulse (398 nm) produced by frequency-doubling of a fraction of the probe-pulse beam is used to create a population in the first electronically excited state of DANS prior to hybrid fs/ps CARS probe interaction.<sup>2</sup> All hybrid fs/ps CARS spectra described here are taken under conditions where the electronic excitation pulse precedes the pump/Stokes time-overlapped pair by 700 fs. A low-resolution spectrometer (Ocean Optics USB-2000) is used to spectrally resolve the outgoing CARS signal from this electronically excited state.

## III. GENERAL THEORETICAL CONSIDERATIONS

We begin by exploring the homodyne-detected CARS signal observed following interaction of a molecular species with three input (optical) electric-field pulses, enumerated 1, 2, and 3 to represent, respectively, the pump, Stokes, and probe pulses. This CARS signal,  $S_{\text{CARS}}$ , described in the frequency domain as a function of signal frequency ( $\omega_S$ ) and delays ( $\tau_{12}$  and  $\tau_{23}$ ) between pairs of pulses—where we follow the standard convention that  $\tau_{mn} > 0$  when the peak of pulse  $n$  arrives after the peak of pulse  $m$ —is assumed to result from both NR and resonant complex third-order polarization [ $P^{(3)}$ ] components as follows:<sup>51</sup>

$$S_{\text{CARS}}(\omega_S, \tau_{12}, \tau_{23}) \propto \left| P_{\text{NR}}^{(3)}(\omega_S, \tau_{12}, \tau_{23}) + P_{\text{CARS}}^{(3)}(\omega_S, \tau_{12}, \tau_{23}) \right|^2. \quad (1)$$

In this expression, the resonant frequency-domain CARS component,  $P_{\text{CARS}}^{(3)}(\omega_S, \tau_{12}, \tau_{23})$ , is the inverse Fourier transform (IFT) of the induced time-domain complex

polarization,

$$P_{\text{CARS}}^{(3)}(t, \tau_{12}, \tau_{23}) = \left( \frac{i}{\hbar} \right)^3 \int_0^\infty dt_3 \int_0^\infty dt_2 \int_0^\infty dt_1 \{ R_4(t_3, t_2, t_1) \times E_3(t - t_3) E_2^*(t + \tau_{23} - t_3 - t_2) \times E_1(t + \tau_{23} + \tau_{12} - t_3 - t_2 - t_1) \times e^{i(\omega_1 - \omega_2 + \omega_3)t_3} e^{i(\omega_1 - \omega_2)t_2} e^{i\omega_1 t_1} \}, \quad (2)$$

where  $E_1(t)$ ,  $E_2(t)$ , and  $E_3(t)$  represent the complex time-domain electric-field envelopes and  $\omega_1$ ,  $\omega_2$ , and  $\omega_3$  represent the carrier frequencies associated with the three enumerated pulses, whereas  $R_4$  (following the numbering conventions used in Ref. 51) is the relevant third-order response function that survives the rotating-wave approximation (RWA) by virtue of Raman-active molecular resonances present near the pump–Stokes difference frequency,  $(\omega_1 - \omega_2)$ .<sup>51</sup> Within the Eq. (2) expression, the integration variables,  $t_1$ ,  $t_2$ , and  $t_3$ , reflect coherence timescales separating field interactions (as depicted in the wave-mixing energy-level diagram in Fig. 1), and the CARS carrier frequency,  $\omega_{\text{CARS}} = \omega_3 - \omega_2 + \omega_1$ , associated with this detected polarization in the time domain,  $t$ , has been suppressed.

The three integration domains in Eq. (2), when integrated numerically, can result in time-consuming computations; therefore, it is often beneficial to simplify this expression when warranted by the experimental system. In particular, a large detuning of pulses 1 and 3 from electronic resonance in the molecular species of interest, as depicted in Fig. 1, results in a nearly instantaneous effective molecular dephasing over both the  $t_1$  and  $t_3$  timescales. Thus, in these calculations, the third-order response function over each of these timescales is assumed to be fast compared to the time dependence of the pulse electric-field envelopes, such that  $R_4(t_3, t_2, t_1) \approx \delta(t_3)R_4(0, t_2, 0)\delta(t_1)$ , where the reduced-dimensionality third-order time-domain response function takes the form

$$R_4(0, t_2, 0) = \sum_{a,c} I_{ca} \theta(t_2) e^{-i\omega_{ca}t_2 - \Gamma_{ca}t_2}. \quad (3)$$

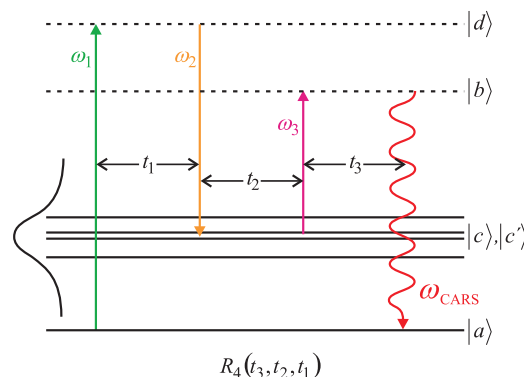


FIG. 1. Wave-mixing energy-level diagram depicting the third-order response function,  $R_4(t_3, t_2, t_1)$  that dominates time-resolved CARS signals. Solid vertical arrows represent field interactions with pulses 1, 2, and 3, whereas the wavy arrow represents the emitted CARS field resulting from energy conservation. Elapsed times between successive field interactions are represented by the variables  $t_1$ ,  $t_2$ , and  $t_3$ .

In this expression, the summation is carried out over initial states  $|a\rangle$  and accessible Raman active states  $|c\rangle$ ,  $I_{ca}$  is a typically Boltzmann-statistics-weighted transition intensity that further encompasses transition-dipole-moment products associated with the contributing electronic transitions,  $\theta(t)$  is a Heaviside step function reflecting the causality requirement, and  $\omega_{ca}$  and  $\Gamma_{ca}$  are, respectively, the Bohr frequency and the dephasing rate associated with the  $|c\rangle \leftarrow |a\rangle$  transition.<sup>51</sup> For gas-phase species such as  $N_2$ , the computational determination of  $I_{ca}$ ,  $\omega_{ca}$ , and  $\Gamma_{ca}$  is detailed in Appendix A. Under these assumptions of instantaneous electronic dephasing, Eq. (2) reduces to

$$P_{\text{CARS}}^{(3)}(t, \tau_{12}, \tau_{23}) = \left(\frac{i}{\hbar}\right)^3 E_3(t) \int_0^\infty dt_2 \cdot \{R_4(0, t_2, 0) \cdot E_2^*(t + \tau_{23} - t_2) \times E_1(t + \tau_{23} + \tau_{12} - t_2) \cdot e^{i(\omega_1 - \omega_2)t_2}\}, \quad (4)$$

Upon application of a Fourier transform to describe the frequency-domain signal, the third order polarization then takes the form

$$P_{\text{CARS}}^{(3)}(\Delta, \tau_{12}, \tau_{23}) = \frac{1}{\sqrt{2\pi}} \left(\frac{i}{\hbar}\right)^3 \int_{-\infty}^\infty dt \cdot E_3(t) e^{i\Delta t} \times \int_0^\infty dt_2 \cdot \{R_4(0, t_2, 0) \cdot E_2^*(t + \tau_{23} - t_2) \times E_1(t + \tau_{23} + \tau_{12} - t_2) \cdot e^{i(\omega_1 - \omega_2)t_2}\}, \quad (5)$$

where  $\Delta = (\omega_S - \omega_{\text{CARS}})$  represents detuning relative to the carrier CARS frequency,  $\omega_{\text{CARS}}$ , defined above. Finally, in typical tr-CARS experiments, the delay between the peaks of pulses 1 and 2 is held at zero; therefore,  $\tau_{12} = 0$  will be assumed in further discussion.

It should be noted that the NR frequency-domain component in Eq. (1) can be expressed using the IFT of an analogous expression to Eq. (2) that contains multiple strongly contributing molecular optical third-order response functions ( $R_1$  through  $R_4$ ), each of which can play varying roles in the overall NR signal.<sup>52</sup> This NR contribution, which typically contributes a broad, featureless component to frequency-domain experimental spectra, can be viewed as a local oscillator that provides significant enhancement of the resonant CARS signal of interest via a heterodyne cross term of the form  $P_{\text{NR}}^{(3)} \cdot P_{\text{CARS}}^{(3)}$ . In practice, however, it is often difficult to quantify the relative contributions of each of these optical pathways, and this, in turn, makes it challenging to model accurately the structured phase and amplitude of the NR contribution. Thus, many time-resolved experimental approaches, including hybrid fs/ps CARS, have been devised particularly to reduce or remove these NR contributions, which dominate only when the electric fields from the three contributing pulses overlap in time. Since the emphasis in these experiments is on the effects of various probe-pulse shapes and delays in removing this contaminating NR contribution, rather than on precise

modeling of the shape and relative phase of the NR signal, a simplified expression for the NR contributions involving only the  $R_4$  response function are considered as a surrogate for the total NR contribution. Thus, the numerically calculated CARS signal, containing both NR and resonant contributions, is expressed using Eq. (1), in which the expression for  $P_{\text{NR}}^{(3)}(\omega_S, \tau_{12}, \tau_{23})$  is identical to the  $P_{\text{CARS}}^{(3)}(\omega_S, \tau_{12}, \tau_{23})$  expression described in Eq. (5), with the exception that the reduced-dimensionality third-order response function,  $R_4(0, t_2, 0)$ , is replaced by a single, rapidly decaying term ( $\Gamma_{\text{NR}} \gg \Gamma_{ca}$ ) described by

$$R_{\text{NR}}(0, t_2, 0) = I_{\text{NR}} \theta(t_2) e^{-\Gamma_{\text{NR}} t_2}, \quad (6)$$

where the NR intensity scalar,  $I_{\text{NR}}$ , is adjusted to match observed experimental NR contributions.

Before exploring several limiting cases below, one additional assumption can be made to simplify the derived analytical expressions. Assuming that the pulse-1 and pulse-2 intensity envelopes [ $I_1(t) \propto |E_1(t)|^2$  and  $I_2(t) \propto |E_2(t)|^2$ ] are impulsive [i.e.,  $E_1(t)$ ,  $E_2^*(t) \approx \delta(t)$ ] in comparison to the timescales associated with the third-order response during  $t_2$ , Eqs. (3) and (5) can be combined to give

$$P_{\text{CARS}}^{(3)}(\Delta, \tau_{12} = 0, \tau_{23}) = \frac{1}{\sqrt{2\pi}} \left(\frac{i}{\hbar}\right)^3 e^{i(\omega_1 - \omega_2)\tau_{23}} \times \int_{-\tau_{23}}^\infty dt \cdot E_3(t) e^{i(\omega_1 - \omega_2 + \Delta)t} \times \sum_{a,c} I_{ca} e^{-i\omega_{ca}(t + \tau_{23}) - \Gamma_{ca}(t + \tau_{23})}. \quad (7)$$

It is important to emphasize that this simplifying assumption of impulsive pulses 1 and 2 removes the spectral weighting associated with these typically finite-bandwidth pulses; these assumptions are only used to provide simplified analytical expressions for the limiting cases described below and are not made in the numerical simulations of the experimental results.

#### IV. PROBE PULSE-SHAPE EFFECTS

Equation (5) can be readily integrated numerically for arbitrary forms of time-domain electric fields associated with pulses 1–3, and all simulated data included here use this expression in combination with Eq. (1). However, because the emphasis of this work is on describing and understanding the interrelated time and frequency dependence observed in hybrid fs/ps CARS experiments, it is instructive to derive analytical expressions that emphasize several aspects of the time and frequency dependence expected in two limiting cases. These limiting cases include that of a short, well-separated probe pulse, as is used in traditional fs tr-CARS experiments and detailed in Appendix B, and that of a probe pulse with a duration exceeding the decay lifetimes of the molecular system, as is the case in purely frequency-resolved CARS experiments and described in Appendix C. The limiting-case analytical expressions can provide a more intuitive understanding of the time- and frequency-domain CARS signals that are observed in

hybrid fs/ps CARS using frequency-domain probe-pulse filters, such as the commonly used top-hat and Lorentzian spectral filters that are described, respectively, in Secs. IV A and IV B below.

## A. Hybrid fs/ps CARS with square (top-hat) frequency-domain probe pulse

### 1. Theoretical treatment of square probe pulse

Because of the relative ease associated with the necessary rudimentary pulse-amplitude shaping, many of the initial implementations of the hybrid fs/ps CARS probe approach use a narrowband square pulse (i.e., top-hat) spectral profile in the frequency domain.<sup>1-3,5,7-9</sup> Such a pulse spectral shape results in a symmetric time-domain probe pulse with a sinc temporal electric-field profile,

$$E_3(t) = \frac{A \sin\left(\frac{wt}{2}\right)}{t}, \quad (8)$$

where  $A$  represents a pulse peak-amplitude scaling factor and  $w$  corresponds to the spectral width of the amplitude-shaped frequency-domain square pulse. The corresponding time-domain pulse-intensity profile therefore exhibits nodes at  $t = 2k\pi/w$ , where  $k$  is a nonzero integer.<sup>1,6</sup> Although an analytical expression can be derived from Eq. (7) for such a probe pulse when it is coincident in time with the time-overlapped pulses 1 and 2 (i.e.,  $\tau_{23} = 0$ ), more general analytical expressions for arbitrary  $\tau_{23}$  can only be derived by expanding  $E_3(t)$  as a Taylor series about  $t = \tau_{23}$ . Thus, this discussion will focus primarily on numerical simulations as a function of  $\tau_{23}$ , and analytical approximations will only be mentioned briefly for the particular case where the probe-pulse node overlaps the time-coincident pulses 1 and 2 and, therefore,  $\tau_{23} = 2\pi/w$ .

### 2. Simulation of gas-phase hybrid fs/ps CARS experiments

Example experimental and simulated hybrid fs/ps CARS signal for  $N_2$  gas at an adiabatic flame temperature of  $T = 2370$  K are depicted in Fig. 2 for a top-hat probe-pulse spectrum with a spectral width,  $w$ , of  $12.2 \text{ cm}^{-1}$ . Assuming ideal amplitude shaping, this spectral width gives rise to a  $\text{sinc}^2$  time-domain probe-pulse intensity profile containing nodes at non-zero integer multiples of  $2.73$  ps and a temporal FWHM of  $2.42$  ps [Eq. (8)]. The contour plot data in Fig. 2 represent the spectrally resolved hybrid fs/ps CARS signal, plotted as a function of anti-Stokes shift relative to the central probe-pulse frequency, at a range of probe-pulse delays from  $-5$  ps to  $105$  ps with a  $1$ -ps time-step size; both experimental and simulated results are shown. The amplitude and relative phase of the NR contributions in the simulated results have been optimized using a least-squares fitting procedure, and the simulated spectra have been convolved with a Gaussian (FWHM =  $1.8 \text{ cm}^{-1}$ ) instrument-response function. These results generally exhibit a maximum spectral intensity, dominated by interference associated with NR contributions,

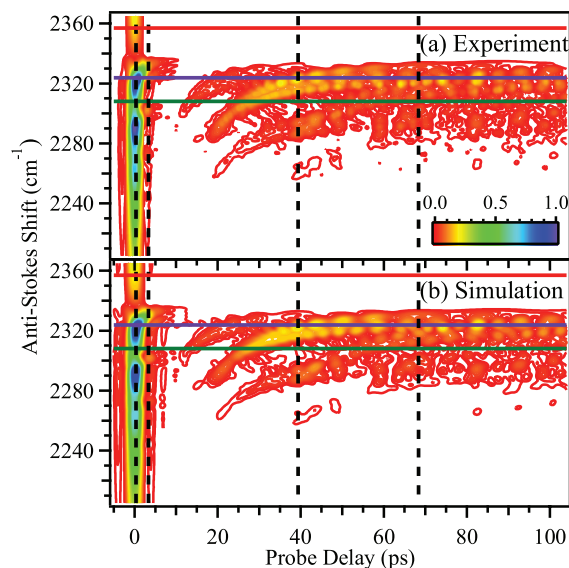


FIG. 2. Comparison of time-dependent experimental (a) and simulated (b) hybrid fs/ps CARS vibrational  $N_2$  spectra at  $T = 2370$  K. Contour plots (linear color scale shown) depict the observed frequency- and time-resolved spectra. Vertical dashed lines at 0, 3, 39, and 68 ps represent specific time-delayed spectra that are discussed in further detail in the text. Horizontal lines at  $2308 \text{ cm}^{-1}$  and  $2324 \text{ cm}^{-1}$  correspond, respectively, to slices through the high- $J$  and low- $J$  regions of the  $N_2 v = 1 \leftarrow v = 0$  manifold.

at a 0-ps probe delay and unique delay-dependent spectral profiles at positive probe delays. A clear frequency sweep of multiple peaks from low to high frequencies is also observed as probe time delay increases. From the point of view of this full time- and frequency-resolved comparison, excellent agreement is observed between the experimental and simulated results over this entire delay range; together, these results provide insight into the physics associated with the observed time-domain results.

Several individual line-out cuts of this contour plot are shown in Fig. 3 depicting the spectral evolution as a function of probe delay. At a probe delay of 0 ps, interference between resonant and strong NR contributions gives rise to a broad spectrum exhibiting peaks associated with vibrationally resolved  $Q$ -branch transitions initiating from several vibrational levels populated at 2370 K ( $Q_v$  transitions initiating from  $v = 0-3$  are clearly observed in the experimental results). Although the simulated results provide a good qualitative match to the 0-ps-delay experimental results, it is clear that, because of the challenges associated with accurate modeling of the interference between the resonant and NR contributions, the modulation depths and relative peak intensities of the vibrational transitions are difficult to reproduce quantitatively while simultaneously fitting the long-delay results. Coupled with the fact that the intensities and relative phases of the NR contributions depend heavily on the temperature-dependent number densities of all species present, this further emphasizes the need to minimize NR contributions in quantitative diagnostic approaches based on this technique. At longer delays, including the 3-ps, 39-ps, and 68-ps data shown in Fig. 3, the observed spectra clearly exhibit structures that maintain similar relative vibrational-manifold intensities and spacing yet include additional delay-dependent

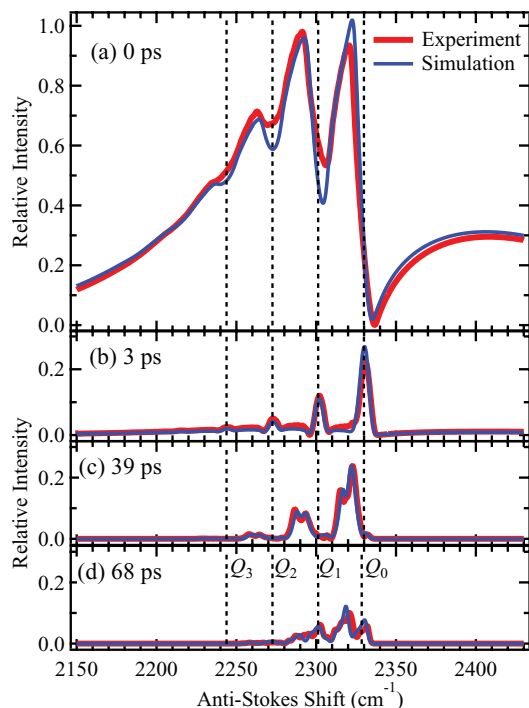


FIG. 3. Comparison of experimental and simulated hybrid fs/ps CARS vibrational  $N_2$  spectra at  $T = 2370$  K at probe delays of (a) 0 ps, (b) 3 ps, (c) 39 ps, and (d) 68 ps; all signals are normalized to the peak of the 0-ps probe-delay spectrum. Vibrational bandheads (dashed vertical lines) corresponding to the  $J = 0$   $Q$ -branch transition are labeled as  $Q_v$  for each  $v+1 \leftarrow v$  transition.

rotational substructure. For example, the spectrum observed at 3 ps, which corresponds approximately to the delay at which the first node of the probe-pulse intensity profile overlaps the time-coincident pump/Stokes pulse pair, exhibits minimal NR background and well-resolved peaks centered at the  $J = 0$  vibrational bandheads. As discussed in previous work,<sup>1,3,6</sup> this particular probe delay is ideal for minimizing contaminating contributions from NR background, which are only present during delays in which the probe-pulse intensity overlaps the time-synchronous pump/Stokes pulses. Furthermore, under experimental conditions associated with gas-phase diagnostic measurements, it is often important to *minimize* the delay between the pump/Stokes pair and the probe pulse to reduce the effects of collisional decay processes since the concentrations and identities of colliding partners are often not known. Thus, these 3-ps-delay data represent an optimal compromise that allows detection of spectra essentially free of NR background while exhibiting no collision-dependent behavior at pressures as high as 20 bars.<sup>9,10,53</sup> Still, the changes in spectral profiles observed in the 39-ps- and 68-ps-delay data emphasize that much of the spectral information observed within the hybrid fs/ps CARS signal is contained in the time-dependent nature of this signal. Whereas these longer delay spectra contain coarse peaks associated with the same vibrational transitions observed in the 3-ps data, a unique fine structure is observed within the spectra at each of these delays, with the 39-ps data emphasizing mid-range rotational  $Q$ -branch frequencies and the appearance of bimodal rotational structure with peaks near  $J \approx 22$  and  $J \approx 28$ . Similarly, the 68-ps data exhibit a more

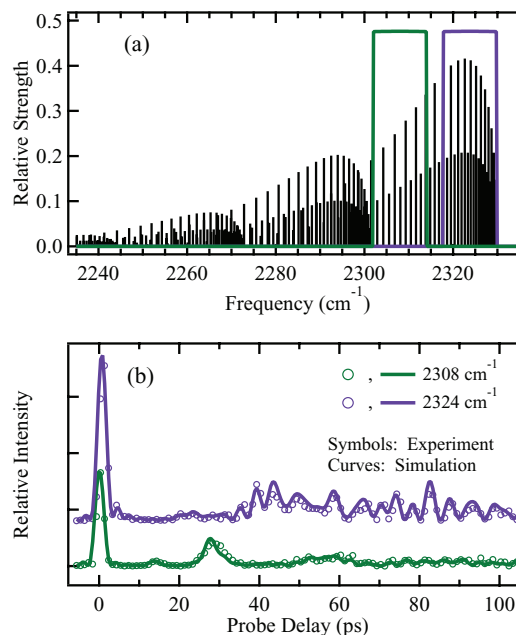


FIG. 4. (a) Stick spectrum of contributing  $N_2$   $Q$ -branch rovibrational transitions; square pulse spectra represent regions spanned by experimental frequency-domain top-hat pulse. (b) Probe-delay-dependent experimental and simulated hybrid fs/ps CARS signals observed at  $2308$   $cm^{-1}$  and  $2324$   $cm^{-1}$ , which consist of coherent signal arising from, respectively, high- $J$  and low- $J$   $Q_0$  transitions selected by the frequency-domain square probe pulse.

notable bimodal rotational fine structure that includes a peak near the  $J = 0$  vibrational bandhead and an additional peak near the frequencies corresponding to  $J \approx 30$ .

The simultaneous time and frequency dependence of the observed hybrid fs/ps CARS signal can be explored further by examining frequency-dependent line-out cuts of the full two-dimensional signal shown in Fig. 2. Two examples of this appear in Fig. 4, where the experimental time-domain signals centered at two anti-Stokes-shifted frequencies ( $2308$   $cm^{-1}$  and  $2324$   $cm^{-1}$ ) are shown. Fig. 4(a) shows the positions of these frequencies—depicted as top-hat spectral profiles centered at these two frequencies and exhibiting widths ( $w = 12.2$   $cm^{-1}$ ) equal to that of the narrowband amplitude-shaped probe pulse—with respect to the  $N_2$  molecular rovibrational transitions of interest; the corresponding time-domain signals associated with these two frequencies are shown in Fig. 4(b). Such a comparison emphasizes the features that contribute to the time-domain spectral signatures observed at different frequencies using this amplitude-shaped narrowband pulse. In particular, the probe-pulse frequency-domain window used in this hybrid fs/ps CARS scheme serves as a spectral filter of the rovibrational levels that contribute to the time-domain signal at a given anti-Stokes frequency. Both examples in Fig. 4(b) exhibit complex but different rotational-recurrence structures that also differ significantly from the highly regular time-domain structure observed in pure time-resolved rotational CARS (RCARS).<sup>21,54</sup> In RCARS, the energy spacing between adjacent rotational  $S$ -branch transitions is nearly constant<sup>10</sup>—exhibiting, in most cases, only small deviations from the  $4B_0$  prediction associated with the rigid-rotor approximation, where, to first

order,

$$B_v = B_e - \alpha_e(v + 1/2), \quad (9)$$

and  $\alpha_e$  is the (first-order) vibration–rotation coupling constant that serves as a correction to the rigid-rotor rotational constant—and the corresponding time-domain CARS signal exhibits short, equally spaced partial and full recurrence peaks that can be correlated to the classical molecular rotational period,  $\tau_{\text{rot}} \sim (2B_0)^{-1}$ .<sup>10</sup> In contrast,  $Q$ -branch vibrational-transition spacings depend, via  $\alpha_e$ , on the difference in rotational constants associated with the two contributing vibrational levels and exhibit a spacing between adjacent  $Q$ -branch lines that increases approximately linearly with  $J$ . This generally results in the more complex time-dependent signatures observed in fs vibrational CARS experiments<sup>21,22</sup> that are emphasized further by the frequency-windowing characteristics associated with the probe-pulse top-hat profile. The data centered at a  $2324 \text{ cm}^{-1}$  anti-Stokes shift, for example, result from a series of closely spaced  $Q$ -branch transitions ranging from  $J = 0$  to  $J \approx 26$  and corresponding energy spacings between adjacent transitions ranging, approximately linearly with  $J$ , from  $0.03 \text{ cm}^{-1}$  to  $0.90 \text{ cm}^{-1}$  within the  $12.2 \text{ cm}^{-1}$  probe spectral window; this gives rise to irregular oscillations associated with many partial recurrences between various subsets of these contributing states during the 100-ps delay range shown in Fig. 4(b). The data centered near  $2308 \text{ cm}^{-1}$ , in contrast, result instead from a smaller number of  $Q$ -branch transitions associated with  $J \approx 30$  to  $J \approx 40$ , where the spacing between adjacent transitions becomes more regular (ranging from  $1.07 \text{ cm}^{-1}$  to  $1.39 \text{ cm}^{-1}$ ). This increased regularity is apparent in the time-domain signal, which exhibits fewer, more pronounced recurrences, most obviously near 28 ps but also more weakly observed near 14 ps; these correspond roughly to half and quarter recurrences, respectively, that would be observed in a system containing exactly equally spaced transitions, albeit with corresponding timescales associated with the vibration–rotation coupling constant rather than with the rotational constant that gives rise to the correspondence between RCARS recurrences and classical rotational timescales. Despite the relative sparseness of the transitions within this spectral window, the variation in spacing between adjacent transitions still results in a frequency-spread broadening of the corresponding “full-recurrence” peak near 56 ps, and the time-domain signal at longer delays resembles the more irregular oscillatory behavior observed in the low- $J$  spectrally windowed results.

### 3. Simulation of condensed-phase experiments and square-probe-pulse lineshape implications

To explore further the notable lineshape/linewidth effects associated with the top-hat-shaped narrowband probe pulse that are observed in the gas-phase  $\text{N}_2$  experiments as the pulse-3 delay changes, a condensed-phase system was chosen that exhibits a rapid dephasing comparable to the experimentally accessible hybrid fs/ps CARS probe-pulse durations. In particular, studies of the time-evolving electronically excited state of DANS solvated in ACN provide an excellent system to test the relationships between observed linewidths

and corresponding molecular dephasing timescales. Initial electronic excitation accesses an electronic state that is often termed a “locally excited” state, which, in the presence of a polar solvent, evolves on timescales associated with solvation to form an energetically stabilized long-lived intramolecular charge-transfer (ICT) state. This ICT state of DANS exhibits a significant number of strong Raman-active vibrational resonances as compared to the NR contribution as well as the corresponding ground-state DANS CARS signal; this makes the excited-state signal particularly amenable to exploring effects of pulse-3 delays on lineshapes. All experiments described here involve initiation of the hybrid fs/ps CARS probe process via time-overlapped pump/Stokes pulses at a delay of 700 fs after impulsive excitation of DANS with a 398-nm pulse. A top-hat amplitude mask ( $w = 15.4 \text{ cm}^{-1}$ ) is used to produce the ps-duration probe pulse. A sample experimental spectrum at a probe-pulse delay of  $\tau_{23} = 2\pi/w = 2.15 \text{ ps}$ , which corresponds to the delay at which the first node of the probe pulse overlaps the time-overlapped pump/Stokes pair, is depicted in Fig. 5. The observed signal exhibits eight resolvable peaks in the  $1000\text{--}1700 \text{ cm}^{-1}$  fingerprint spectral region. The temporal evolution of this detected hybrid fs/ps CARS signal is shown as a contour plot in Fig. 6. The simulated signal in Fig. 6(b) is calculated following a least-squares fitting of the experimental results at nine distinct probe-pulse delays ranging from  $-2 \text{ ps}$  to  $3 \text{ ps}$ ; the resultant simulated signal is subsequently further convolved with a Gaussian (FWHM =  $13 \text{ cm}^{-1}$ ) spectral-response function to match experimental conditions. The simulated signal depicted in Fig. 5 corresponds to this convolved result at a probe-pulse delay of 2.15 ps. The  $R_4$  third-order-response parameters [Eq. (3)] for the eight vibrational modes used in these simulations are included in Table I.

Most notable in the contour plots presented in Fig. 6 is the similarity in the temporal profiles of the contributing peaks to the symmetric sinc<sup>2</sup> intensity profile of the probe pulse; however, it is also clear that some asymmetry exists with respect to  $\tau_{23} = 0$  in the temporal profiles of the contributing peaks. It is further observed that the linewidths, lineshapes, and relative intensities of the contributing Raman modes vary significantly with probe-pulse delay. These effects are emphasized in Fig. 7, which depicts the observed linewidths (FWHM) and peak intensity profiles associated with the peaks labeled as

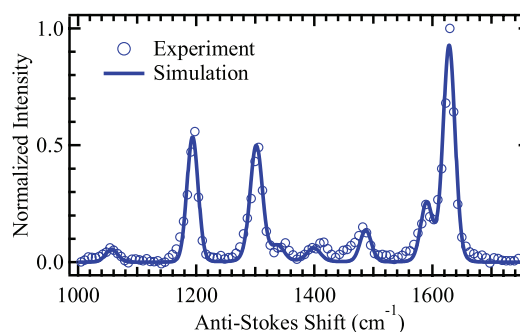


FIG. 5. Comparison of experimental (symbols) and simulated (curve) excited-state DANS hybrid fs/ps CARS spectra at a probe delay of 2.15 ps, in which the first node of the probe-pulse intensity spectrum overlaps the pump/Stokes coincident pair. Simulation curve is derived from least-squares fitting of DANS signal at multiple probe delays.

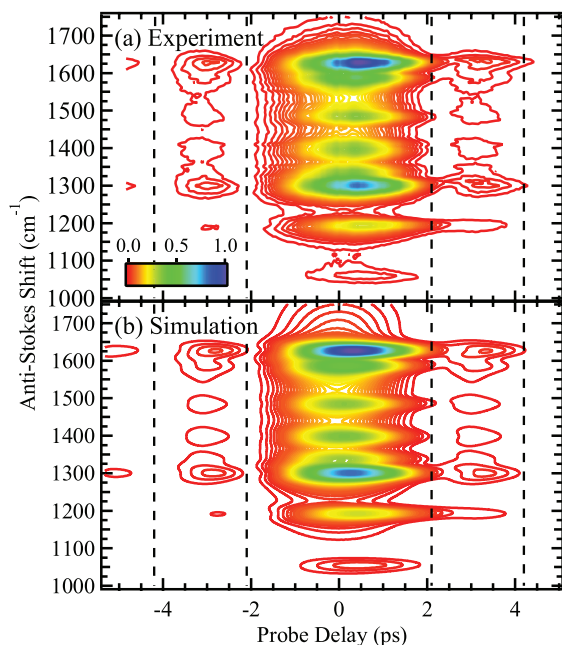


FIG. 6. Comparison of time-dependent experimental (a) and simulated (b) hybrid fs/ps CARS spectra of excited-state DANS using an amplitude-shaped top-hat probe pulse with  $w = 15.4 \text{ cm}^{-1}$ . Contour plots (linear color scale shown) depict the observed frequency- and time-resolved spectra. Vertical dashed lines represent delays,  $\tau_{23} = 2k\pi/w$ , at which nodes of the  $\text{sinc}^2$  probe-pulse intensity coincide temporally with the CARS initiation pulses; non-resonant contributions to the signal are observed to be minimized at these delays.

modes 2 and 3 in Table I. These linewidths and intensities have been determined via least-squares fitting of individual peaks to Lorentzian lineshapes. As will be discussed below, the lineshape for a given molecular transition is not necessarily expected to exhibit a Lorentzian profile at all probe delays, in some cases exhibiting two separate peaks and poorer agreement between experiment and simulation, such as in the  $\tau_{23} = -2 \text{ ps}$  to  $\tau_{23} = -1$  region and the  $\tau_{23} = 2.5 \text{ ps}$  to  $\tau_{23} = 3.5 \text{ ps}$  region in Figs. 7(a) and 7(b). Thus, this particular functional form is only used to provide a simplified quantification of the observed linewidths and further comparison of experimental and simulated results. For the simulated results, linewidths both before and after convolution with the spectral-response function are included. From these results, it is clear that there is a notable line-narrowing effect associ-

TABLE I. Molecular parameters used in simulations of excited-state DANS in ACN.

Mode #	$\omega_{ca} \text{ (cm}^{-1}\text{)}$	$\Gamma_{ca} \text{ (cm}^{-1}\text{)}$	$I_{ca}$
1	1057.0	7.9	0.41
2	1194.0	5.0	0.60
3	1302.1	8.7	0.85
4	1337.8	7.2	0.23
5	1399.0	10.5	0.33
6	1487.0	5.1	0.15
7	1589.9	6.3	0.35
8	1628.2	7.8	1.0

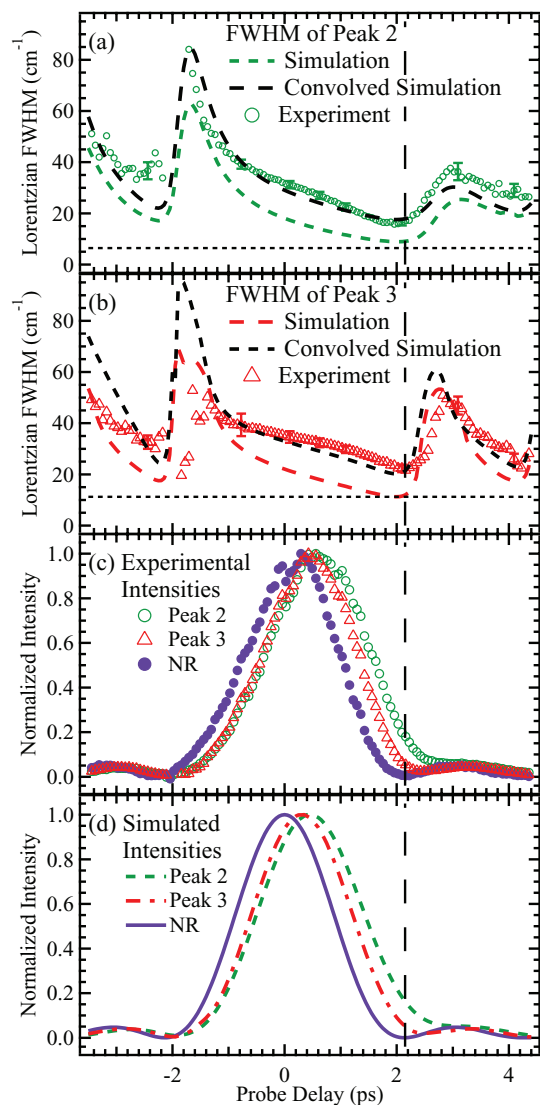


FIG. 7. Peak widths and intensities vs. top-hat probe-pulse delay; dashed vertical line corresponds to delay at which the first temporal node of the probe pulse coincides with the time-overlapped pump and Stokes pulses. (a) and (b) Measured Lorentzian FWHM for experimental (symbols) and simulated (dashed curves) peak-2 and peak-3 signals, respectively; simulated signals calculated with (black curve) and without (color curve) convolution with an instrument spectral-response function. Horizontal dotted lines in (a) and (b) represent  $1.287 \cdot \Gamma$  for each corresponding vibrational mode. (c) and (d) Normalized intensities for experimental (c) and simulated (d) peaks 2 and 3 and NR contributions to signal.

ated with positive delays of the probe pulse as compared to the measured linewidth at  $\tau_{23} = 0$ , and the  $\tau_{23} = 2\pi/w$  delay corresponds to the narrowest linewidth; this narrowing effect is observed for all eight peaks, including the two depicted in Fig. 7. Similarly, the intensity profiles associated with the peaks exhibit time-dependent behaviors that are, in turn, dependent on the magnitudes of the corresponding decay constants. For the experimental results, the spectral intensity at  $1535 \text{ cm}^{-1}$  was used as an indication of the purely NR CARS signal, which corresponds approximately to a cross-correlation of the impulsive pump/Stokes pulse pair with the  $\text{sinc}^2$  probe-pulse intensity distribution. In contrast, the intensity profiles associated with the resonant peaks have similar

$\text{sinc}^2$  temporal behaviors that are, however, shifted toward positive delays as compared to the NR signal. Moreover, the magnitude of the time shift is nearly equal to the corresponding CARS decay time constant,  $\tau_{ca}$ , associated with the decay constant  $\Gamma_{ca}$ ,<sup>55</sup> resulting in a notable change in the ratio of peak intensities as a function of probe-pulse delay for peaks with different decay constants.

As above, the availability of accurate simulation of the observed results provides valuable additional insight into the effects of the components of the third-order response function and probe-pulse delay on the observed signal; in particular, simulations of the results in Fig. 6 can illuminate the lineshape behavior observed in experiments. For example, the simulations can provide insight into the limiting behavior associated with the minimization of NR contributions and narrowing of linewidths that occurs when the node of the probe pulse coincides with the pump/Stokes pair. A comparison of simulated spectra associated with a single molecular transition is depicted in Fig. 8, where only the best-fit molecular parameters associated with the NR and peak-3 contributions are included. The real component of the calculated third-order response function,  $R_4(0, t_2, 0)$ , for this model system is shown in Fig. 8(a) to emphasize the timescales associated with the NR contributions (short, nearly impulsive peak near  $t = 0$ ) and the resonance. Fig. 8(b) depicts the magnitude of the simulated probe-pulse electric field at three discrete probe-pulse delays. The resultant time-domain third-order polarizations and simulated CARS signal are shown, respectively, in Figs. 8(c) and 8(d). These simulations illustrate the effects of the probe-pulse delay,  $\tau_{23}$ . At  $\tau_{23} = 0$ , the outgoing polarization signal contains a modulated time-domain signal that nearly mimics the decay timescale of the full third-order response function, and the corresponding frequency-domain CARS signal contains both a broad (although relatively weak, as noted above) NR contribution spanning the bandwidth associated with the overlapped pump and Stokes pulses and a narrower resonant peak that exhibits some asymmetry resulting from interference with the NR contributions. The FWHM of this peak is approximately  $23.7 \text{ cm}^{-1}$ , which is somewhat larger than the  $2 \cdot \Gamma_{ca} = 17.4 \text{ cm}^{-1}$  FWHM expected in the long-probe-pulse limit; this broadened linewidth results from the fact that the probe electric field falls to zero, reaching the first positive node during the timescale of the third-order response function and resulting in a comparatively dampened time-domain third-order polarization.

In contrast, the third-order polarization associated with the electric field at  $\tau_{23} = 2\pi/w = 2.15 \text{ ps}$  exhibits notably different features, including the nearly complete removal of impulsive NR contributions to the outgoing signal. Moreover, the electric-field magnitude is increasing approximately linearly during the timescale of exponential decay of the response function; the composite result is a time-domain polarization that dampens the early-timescale behavior but emphasizes the longer timescale behavior of the third-order response function. The corresponding frequency-domain CARS signal, therefore, exhibits negligible NR contributions and a narrower resonant peak. In fact, when used at a delay of  $\tau_{23} = 2\pi/w$ , the sinc time-domain electric field described in Eq. (8) can be written as a Taylor expansion in the

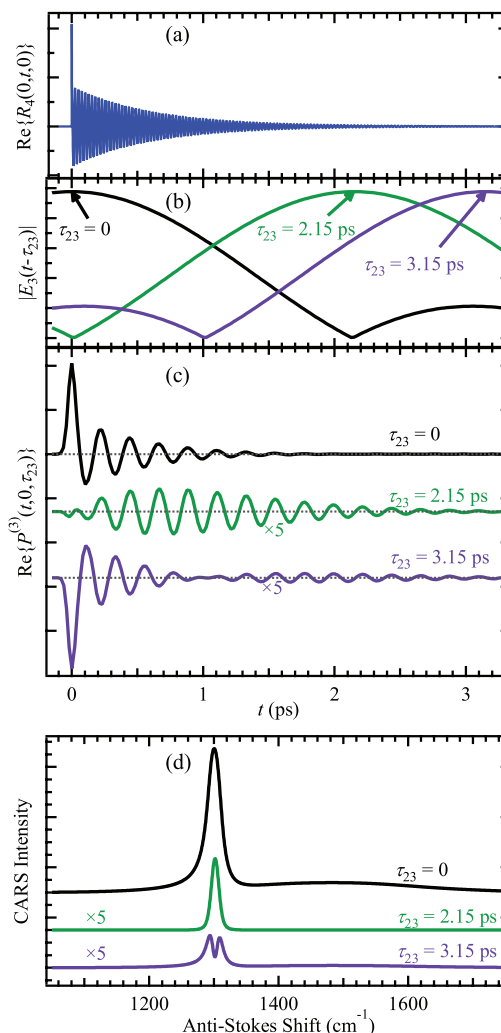


FIG. 8. Simulated lineshape dependence of peak 3 on probe-pulse delay. (a) Real component of the third-order response function,  $R_4(0,t,0)$ , consisting of contributions from non-resonant signal and this single mode; oscillations correspond to the peak resonance frequency. (b) Probe-pulse electric-field magnitude at three  $\tau_{23}$  values. (c) Real component of the time-dependent third-order polarizations associated with these three probe-pulse delays; oscillation frequency represents the detuning of the resonance relative to  $(\omega_1 - \omega_2)$ . (d) Calculated CARS signal intensity resulting from these three probe-pulse delays. Curves in (c) and (d) have been offset for clarity.

form

$$E_3\left(t - \frac{2\pi}{w}\right) = a_1 t + \frac{1}{2} a_2 t^2 + \dots, \quad (10)$$

where  $a_1 = Aw^2/4\pi$  and  $a_2 = Aw^3/4\pi^2$ . In the limit that this expansion is truncated at the linear term, introduction of  $E_3(t)$  into Eq. (7) results in an analytical expression for the outgoing signal of

$$S_{\text{CARS}}(\omega_s, \tau_{12} = 0, \tau_{23} = 2\pi/w) \propto \left| \sum_{a,c} I_{ca} \frac{1}{\{(\omega_s - (\omega_{ca} + \omega_3)) + i\Gamma_{ca}\}^2} \right|^2. \quad (11)$$

In the limit of well-separated transitions, this expression results in peaks with Lorentzian lineshapes centered at the anti-Stokes-shifted Raman frequency and exhibiting

linewidths equal to  $2\sqrt{\sqrt{2}-1}\Gamma_{ca} \approx 1.287 \cdot \Gamma_{ca}$ , narrower than the  $2 \cdot \Gamma_{ca}$  linewidth associated with the long-probe-pulse limit described above; this theoretical limit is shown as horizontal dotted lines in Fig. 7 for peaks 2 and 3. The peak-3 FWHM at the  $\tau_{23} = 2\pi/w$  delay is  $11.3 \text{ cm}^{-1}$ , nearly matching this theoretical limit of  $11.2 \text{ cm}^{-1}$ . It is important to note that, although the use of this particular time-delayed probe—in which the node of the probe pulse coincides with the pump/Stokes pair—results in linewidths that are narrower than is dictated by the decay timescale of the third-order response function, this narrowing only results from a reduced sensitivity toward the early parts of the response function afforded by the increasing probe electric field with time. This compromise, therefore, results in reduced relative sensitivity to peaks with larger decay constants at this probe delay, as is clear from Figs. 7(c) and 7(d). In fact, it is exactly this behavior that allows optimal discrimination at this probe delay against NR contributions, which effectively respond with near-infinite decay rates.

Finally, the non-Lorentzian lineshape behavior exhibited at several probe-pulse delays is emphasized by the  $\tau_{23} = 3.15 \text{ ps}$  simulations depicted in Figs. 8(c) and 8(d). In this case, the node of the electric field overlaps the decaying response function, resulting in a corresponding node and sign change within the time-domain third-order polarization. The resulting frequency-domain signal, therefore, exhibits two distinct peaks associated with the Fourier transform of this bimodal time-domain polarization; additionally, some NR contributions are present at this delay, albeit with reduced relative intensity as compared to the  $\tau_{23} = 0$  data.

## B. Hybrid fs/ps CARS with Lorentzian frequency-domain probe pulse

Unlike the symmetric time-domain pulse generated from a top-hat frequency-domain filter, under certain experimental configurations an asymmetric time-domain pulse represents an ideal probe pulse for the hybrid fs/ps CARS optical setup.<sup>10</sup> Most importantly, an asymmetric pulse exhibiting a rapid onset and subsequent near-exponential decay can be used to discriminate significantly against NR contributions—which are present only when the probe electric field temporally overlaps the pump and Stokes electric fields—without the simultaneous suppression of resonant signal contributions, which typically exhibit decay lifetimes comparable to or longer than this probe-pulse decay lifetime. The benefits of such a pulse shape have previously been discussed by Lagutchev *et al.*,<sup>56,57</sup> who recognized the virtues of this probe pulse shape in frequency-resolved vibrational sum frequency generation (SFG) experiments and demonstrated that such a pulse can be readily prepared experimentally with the simple insertion of a Fabry–Pérot étalon into the probe-pulse beam path. The presence of an étalon results in, ideally, a frequency-domain Lorentzian lineshape, the Fourier transform of which is the above-described decaying asymmetric time-domain pulse. This simple approach has more recently been used to provide optimal probe pulse shaping in hybrid fs/ps CARS experiments probing condensed-phase

environments<sup>58</sup> as well as both vibrational<sup>6</sup> and rotational<sup>10,12</sup> gas-phase transitions. The benefits of and comparison between experiment and simulation associated with these asymmetric probe pulses have already been addressed in some detail,<sup>6,10</sup> therefore, only a brief discussion will be included here, focusing on the simple analytical expressions that can be used to express the lineshapes of the observed spectrally resolved signal.

Analytical treatment of a frequency-domain Lorentzian lineshape with a spectral intensity bandwidth (FWHM) of  $2 \cdot \Gamma_{\text{Lor}}$  results in a time-domain pulse electric field with the simple temporal envelope profile

$$E_3(t) = \begin{cases} 0 (t < 0) \\ B e^{-\Gamma_{\text{Lor}} t} (t \geq 0) \end{cases}, \quad (12)$$

where  $B$  represents an amplitude scaling factor. Insertion of a time-delayed probe pulse of this nature into Eq. (7) results in the following expression for the frequency-domain outgoing CARS signal [via Eq. (1)] in cases where  $\tau_{23} > 0$ :

$$S_{\text{CARS}}^{(3)}(\omega_s, \tau_{12} = 0, \tau_{23}) \propto \left| \sum_{a,c} I_{ca} e^{-i\omega_{ca}\tau_{23} - \Gamma_{ca}\tau_{23}} \cdot \frac{1}{-i(\omega_s - [\omega_{ca} + \omega_3]) + (\Gamma_{\text{Lor}} + \Gamma_{ca})} \right|^2. \quad (13)$$

Thus, analogous to the broadband Gaussian probe case described in Appendix B, the outgoing CARS signal consists of a series of peaks centered at anti-Stokes-shifted frequencies,  $(\omega_{ca} + \omega_3)$ . In contrast to the broadband-probe case, however, these peaks, when well-separated, appear as Lorentzian lineshapes with FWHM linewidths equal to  $(2 \cdot \Gamma_{\text{Lor}} + 2 \cdot \Gamma_{ca})$ , which is simply the sum of the shaped-probe laser linewidth and the natural Raman linewidth associated with the spectroscopic transition. Thus, in cases where the molecular decay timescale,  $\tau_{ca} = (2\pi c \Gamma_{ca})^{-1}$ , in which the multiplicative variable  $c$  is the speed of light, is long compared to the shaped-laser-pulse decay time constant, the observed spectral lineshapes will be dominated by the linewidth of the probe pulse; this will be true at atmospheric pressure in most gas-phase experiments, where collisional dephasing occurs on timescales of tens to hundreds of ps.<sup>25,59</sup> However, in cases in which the molecular decay timescale is fast compared to the probe decay time, as would be the case in most condensed-phase and potentially in high-pressure gas-phase CARS measurements,<sup>53</sup> the spectral linewidths measured in the outgoing CARS signal will be dominated by these natural Raman linewidths.

In cases where there is partial or complete overlap between adjacent Raman-active transitions, the  $\tau_{23}$ -dependent accumulated phases associated with the oscillatory exponential term within the summation in Eq. (13) result in a similar transition-frequency-dependent interference as discussed in the Gaussian-probe-pulse example in Appendix B. Such interference effects have been observed and discussed in detail in hybrid fs/ps rotational CARS experiments using an étalon-shaped probe pulse.<sup>10</sup> It is interesting to note that, in cases in which  $\tau_{23} < 0$  (i.e., the peak of the probe pulse precedes the

peaks of the time-overlapped pump and Stokes pulses), the outgoing CARS signal derived by combining Eqs. (1), (7), and (12) takes the form

$$S_{\text{CARS}}^{(3)}(\omega_s, \tau_{12} = 0, \tau_{23}) \propto e^{2\Gamma_{\text{Lor}}\tau_{23}} \left| \sum_{a,c} I_{ca} \cdot \frac{1}{-i(\omega_s - [\omega_{ca} + \omega_3]) + (\Gamma_{\text{Lor}} + \Gamma_{ca})} \right|^2. \quad (14)$$

Thus, probe-delay-dependent oscillations associated with regions of peak overlap are not expected to occur in these negative  $\tau_{23}$  cases; instead the only time-dependent component of this resonant CARS signal is an exponential decay of the total signal intensity with increasing magnitude of the negative  $\tau_{23}$  value.

## V. CONCLUSIONS

The theoretical and computational details associated with a time- and frequency-domain model of time-dependent CARS have been described and applied toward two different experimental systems, including a gas-phase species ( $\text{N}_2$ ) and a solvated species (DANS) in the condensed phase. The CARS model discussed here is robust in the sense that it can be extended to all tr-CARS approaches involving combinations of sub-ns-duration pulses, including ps-CARS experiments<sup>55,59,60</sup> and the several approaches employing combinations of fs-duration and ps-duration pulses described herein. Here, we have focused discussion on those approaches that employ two broadband initiation pulses—pump and Stokes—and a final probe pulse of varying duration. The probe pulses are generated using specific spectral pulse-shaping schemes, which are applied to the probe pulse to provide both sufficient spectral resolution and pulse temporal profiles that allow discrimination against NR contributions to the CARS signal. These approaches typically exhibit characteristics of both frequency-domain and time-domain signal dependence, and that interrelationship has been explored in detail. Additionally, although this theoretical framework can be readily modified to provide numerical analysis of experimental results in which the ps-duration probe pulse results from extensive chirping of a broadband fs pulse<sup>61</sup>—this configuration has been used, for example, in single-shot gas-phase CARS thermometry experiments<sup>62</sup>—the details of such chirped-probe-pulse simulations have been discussed in Refs. 62–64 and have therefore not been directly addressed here.

The simulations of experimental results that have been included here have all been carried out via numerical integration of the derived expressions for the measured signal. However, additional emphasis has been placed here on the derivation of analytical expressions to describe the observed results. These expressions have been used, in particular, to interpret the purely time-domain and frequency-domain variants of CARS as well as to discuss hybrid fs/ps CARS in which the ps-duration probe pulse is shaped using either a top-hat or a Lorentzian frequency-domain mask. In gas-phase  $\text{N}_2$ , the observed experimental results can be understood in

terms of this intermediate regime, in which some rotational structure within the vibrational manifold is observed both in the time- and frequency-domain signal. The evolution of experimental and modeled  $\text{N}_2$  CARS spectra is compared at various probe-pulse delays, showing excellent accuracy in capturing the temporal dynamics of rovibrational features in high-temperature reacting flows. Simulation of condensed-phase experimental results using a top-hat probe pulse demonstrates that such pulse shaping and delay optimization result in controllable overlap of the time-domain electric field with the decaying third-order response function; this overlap can be manipulated to optimize signal intensity and spectral resolution while discriminating against NR background. Such optimization may be particularly necessary under high-pressure gas-phase conditions, when the timescales for molecular decay become comparable to or faster than the duration of the shaped probe pulse.

## ACKNOWLEDGMENTS

Funding for this research was provided, in part, by the Air Force Research Laboratory under Contract No. FA8650-12-C-2200, the United States Air Force Office of Scientific Research (AFOSR) (Dr. Enrique Parra and Dr. Chiping Li, Program Managers), and the National Science Foundation Early Career program under Contract No. CBET-1056006. J. Miller was funded by the National Science Foundation Graduate Research Fellowship Program, the Department of Defense National Defense Science and Engineering Graduate Fellowship Program, and by a National Research Council Postdoctoral Research Associateship. This work has been cleared for public release (No. 88ABW-2013-3992).

## APPENDIX A: TRANSITION-INTENSITY, FREQUENCY, AND DEPHASING PARAMETERS FOR GAS-PHASE SPECIES

The computational modeling of gas-phase species that are typically used in thermometric applications requires knowledge of accurate molecular transition frequencies ( $\omega_{ca}$ ), Boltzmann-weighted transition strengths ( $I_{ca}$ ), and collisional dephasing rates ( $\Gamma_{ca}$ ) associated with the relevant Raman-active transitions that serve as input parameters to the third-order response function [Eq. (3)]. The vibrational CARS examples described here are typically dominated by  $Q$ -branch Raman ( $v + 1 \leftarrow v$ ) vibrational transitions, so the discussion below will focus on expressions associated with such  $Q$ -branch transitions. In cases where the simulation of pure rotational CARS ( $S$ -branch transitions) data or the inclusion of  $O$ - and  $S$ -branch transitions within vibrational CARS is necessary, the corresponding expressions for  $O$ - and  $S$ -branch transitions can be included as terms in the response function.<sup>7,10</sup> The molecular transition frequencies,  $\omega_{ca} = \omega_{v+1,J} - \omega_{v,J}$ , associated with these  $Q$ -branch transitions are calculated using spectroscopic constants from recent high-resolution experiments,<sup>65</sup> and the corresponding Raman transition strengths,  $I_{ca} = I_{v+1,J \leftarrow v,J}$ , are accounted for as

follows:

$$I_{ca} \propto \frac{(v+1)}{(\omega_{v+1,0} - \omega_{v,0})} \left(1 - \frac{P_{v+1,J}}{P_{v,J}}\right) \times \left[ F_{iso}(J) + \frac{4}{45} b_{J,J} \left(\frac{\gamma'}{a'}\right)^2 F_{aniso}(J) \right]. \quad (\text{A1})$$

In this expression,  $P_{v,J}$  is the initial  $v$ - and  $J$ -dependent probability distribution of  $\text{N}_2$ ,  $b_{J,J}$  are the  $J$ -dependent  $Q$ -branch Placzek–Teller coefficients, and  $(\gamma'/a')$  accounts for the  $Q$ -branch anisotropy, incorporating the first derivative of the polarizability anisotropy ( $\gamma'$ ) and the first derivative of the average isotropic polarizability ( $a'$ ) of the molecule; in this expression, we assume that  $(\gamma'/a') = 1.199$  (Ref. 66) is constant over the CARS wavelengths observed here. The isotropic and anisotropic terms,  $F(J)$ , in Eq. (A1) represent the corresponding Herman–Wallis factors that account for the effects of vibration–rotation coupling on relative rovibrational peak intensities, and are expressed as<sup>67</sup>

$$F(J) = 1 - \left(\frac{2B_e}{\omega_e}\right)^2 (J)(J+1) \left[ \frac{3}{2}(a_1 + 1) - 4\left(\frac{p_2}{p_1}\right) \right], \quad (\text{A2})$$

where  $B_e$  and  $\omega_e$  are, respectively, equilibrium rotational (1.998  $\text{cm}^{-1}$ ) and vibrational (2358.57  $\text{cm}^{-1}$ ) constants of  $\text{N}_2$ ,<sup>66</sup>  $a_1 = -2.7$  is the first Dunham coefficient in the power-series expansion of the ground state  $\text{N}_2$  molecular potential,<sup>66</sup> and the ratio  $(p_2/p_1)$  involves the first and second coefficients of either the isotropic  $[(p_2/p_1)_{iso} = 0.31]$  or anisotropic  $[(p_2/p_1)_{aniso} = 0.57]$  polarizability expansion of  $\text{N}_2$ .<sup>67</sup> For thermometric applications, it is generally assumed that the state populations obey Boltzmann statistics, such that

$$P_{v,J} = \frac{g_J \exp\left(-\frac{\hbar\omega_{v,J}}{k_B T}\right)}{\sum_{v=0}^{\infty} \sum_{J=0}^{\infty} g_J \exp\left(-\frac{\hbar\omega_{v,J}}{k_B T}\right)}, \quad (\text{A3})$$

where  $k_B$  is Boltzmann's constant and  $g_J$  is a degeneracy term. For  $\text{N}_2$ ,

$$g_J = (2J+1) \cdot 1/2[3 + (-1)^J] \quad (\text{A4})$$

accounts for the 2:1  $J$ -dependent nuclear-spin degeneracy associated with even:odd  $J$  levels.

The temperature and pressure dependence of the collisional dephasing rates,  $\Gamma_{ca}$ , which are typically dominated by collision-induced rotational energy transfer (RET), has been studied experimentally for several combustion-relevant species, including  $\text{N}_2$ ,<sup>8,68–70</sup>  $\text{H}_2$ ,<sup>59,71</sup>  $\text{O}_2$ ,<sup>8,72,73</sup>  $\text{CO}$ ,<sup>74</sup> and  $\text{CO}_2$ .<sup>55</sup> These empirical results, in turn, are typically fit to scaling laws—including the modified exponential gap (MEG) law and several variants of the energy-corrected sudden (ECS) approximation—which allow the state-dependent dephasing rates to be described using a small number of adjustable parameters in computational models. For the  $\text{N}_2$  experiments described here, it is assumed that vibrational dephasing is negligible<sup>75</sup> and that, therefore, the  $J$ -dependent collisional dephasing rates are dominated by the RET rates, which are calculated using a generalized MEG model, although the

computational code is arranged such that other parameterized scaling laws, including the power-gap ECS (ECS-P) and an exponential-gap ECS (ECS-E), can be readily used.<sup>68,76,77</sup> In the MEG model,<sup>68</sup> the pressure- and temperature-dependent rates for upward collisional transitions between states,  $|c\rangle$ ,  $|c'\rangle$ , with respective rotational quantum numbers,  $J_i$  and  $J_j$ , are described by

$$\Gamma_{ji} = p\alpha f(T) \left(\frac{T}{T_0}\right)^{-n} \left(\frac{1 + a\hbar\omega_{v+1,J_i}/k_B T\delta}{1 + a\hbar\omega_{v+1,J_j}/k_B T}\right)^2 \times \exp(-\beta\hbar(\omega_{v+1,J_j} - \omega_{v+1,J_i})/k_B T), \quad (\text{A5})$$

where  $p$  and  $T$  represent pressure and temperature, respectively;  $\alpha$ ,  $\beta$ , and  $\delta$  represent adjustable parameters that are optimized by least-squares fitting of experimental results at  $T_0 = 295$  K; and  $a$  is a species-dependent constant that is fixed at 1.5 for  $\text{N}_2$ . The temperature dependences of the collisional RET rates are accounted for in the exponent  $n$ , which is fixed at 0.5 for  $\text{N}_2$ , and the function,  $f(T)$ , which is given by

$$f(T) = \frac{1 - e^{-m}}{1 - e^{-mT/T_0}}. \quad (\text{A6})$$

In this function,  $m$  represents an additional adjustable parameter to allow optimal simulation of experimentally measured  $J$ -dependent linewidths. For downward transitions, microscopic reversibility is assumed using

$$\Gamma_{ij} = \Gamma_{ji} \frac{2J_i + 1}{2J_j + 1} e^{\hbar(\omega_{v+1,J_j} - \omega_{v+1,J_i})/k_B T}. \quad (\text{A7})$$

The  $\text{N}_2$  simulations described here use values of  $\alpha = 0.023$ ,  $\beta = 1.67$ ,  $\delta = 1.21$ , and  $m = 0.1487$ , which have been optimized using frequency-domain linewidth data over the 0–1 atm pressure range and at temperatures ranging from 295 K to 2200 K.<sup>68,78</sup> The diagonal elements of this relaxation  $\mathbf{\Gamma}$ -matrix, which represent the Lorentzian HWHM of the frequency-domain transitions at pressures where line-mixing effects are negligible, can be expressed by

$$\Gamma_j = \sum_{i \neq j} \Gamma_{ij}. \quad (\text{A8})$$

Under conditions where line-mixing effects are negligible ( $\leq 1$  atm in the case of the high-temperature  $\text{N}_2$  simulations described here),<sup>23,25,53,76</sup> these diagonal elements can be used directly as the rotational-state-dependent  $Q$ -branch decay constants,  $\Gamma_{ca}$ , within the third-order response function [Eq. (3)], where states  $|a\rangle$  and  $|c\rangle$  correspond, respectively, to  $J$  levels within the lower and upper vibrational manifolds associated with  $\Delta v = +1$  vibrational transitions, and vibrational dephasing is neglected. We note that, under high-pressure conditions where it becomes necessary to account for line-mixing effects, the  $\mathbf{G}$ -matrix formalism<sup>23,25,53,76</sup> can be readily applied. Here,  $\mathbf{G}$  represents a block-diagonal matrix containing square submatrices corresponding to each vibrational manifold in the form

$$\mathbf{G}_v = i\omega_{(v,J)}\mathbf{I} - \mathbf{\Gamma}, \quad (\text{A9})$$

where  $\omega_{(v,J)}\mathbf{I}$  represents a diagonal  $n \times n$  matrix ( $J = 0$  to  $J_{\max} = n - 1$ ) containing the  $Q$ -branch rotational transitions of the  $v + 1 \leftarrow v$  vibrational manifold, and  $\mathbf{\Gamma}$  is the  $n \times n$  relaxation

matrix described in Eqs. (A5), (A7), and (A8). Diagonalization of  $\mathbf{G}$  produces a series of eigenvalues containing mixed-level rovibrational transition frequencies,  $\tilde{\omega}_{(v,J)}$ , and decay linewidths,  $\tilde{\Gamma}_J$ , that can be used, respectively, as the input parameters  $\omega_{ca}$  and  $\Gamma_{ca}$  in the response function [Eq. (3)] to simulate the time-dependent CARS signal.<sup>23,25,53,76</sup>

As noted in Sec. III, NR contributions to the observed CARS signal are modeled via a rapidly decaying term in the relevant third-order response function; in particular, a large decay constant (five orders of magnitude larger than the corresponding resonant molecular-transition decay constants) is assumed. For transform-limited excitation pulses, the resonant and NR contributions are expected to exhibit an in-quadrature relationship;<sup>79</sup> however, it is typically observed that non-idealities result in a phase shift between these two contributions that differs from 90°. Thus, the relative intensities and phase relationship between the resonant and NR contributions are generally optimized via a least-squares fitting of experimental spectra obtained under conditions where strong NR contributions are present.

## APPENDIX B: UNSHAPED PROBE PULSE (fs tr-CARS LIMIT)

### 1. Theoretical treatment of fs tr-CARS

Typical fs tr-CARS experiments involve the use of a fs-duration probe pulse with a nearly Gaussian temporal profile. If the pulse-3 electric-field envelope is assumed to have a short, Gaussian temporal profile (FWHM =  $2\sqrt{\ln 2}\tau_G$ , where  $\tau_G$  is a width parameter), then for delays between pulses 2 and 3 (i.e.,  $\tau_{23}$ ) that are longer than the pulse-3 duration, the lower integration limit in Eq. (7) can be set to  $-\infty$ . In this limit, the frequency-domain third-order polarization is

$$\begin{aligned} P_{\text{CARS}}^{(3)}(\Delta, \tau_{12} = 0, \tau_{23}) &= \left(\frac{i}{\hbar}\right)^3 e^{i(\omega_1 - \omega_2)\tau_{23}} \\ &\times \sum_{a,c} I_{ca} e^{-i\omega_{ca}\tau_{23} - \Gamma_{ca}\tau_{23}} \\ &\cdot \tilde{E}_3(\omega_{ca} - \Delta - \omega_1 + \omega_2) \cdot e^{(\Gamma_{ca}^2 \tau_G^2/4)} e^{i(\Gamma_{ca}(\omega_{ca} - \Delta)\tau_G^2/2)}, \end{aligned} \quad (\text{B1})$$

where  $\tilde{E}_3(\omega)$  is the Gaussian frequency-domain pulse-3 electric-field envelope, centered at  $\omega = 0$ , defined by

$$\tilde{E}_3(\omega) = \frac{1}{\sqrt{2\pi}} \int_{-\infty}^{\infty} E_3(t) e^{i\omega t} dt. \quad (\text{B2})$$

Combining Eq. (B1) with Eq. (1) while neglecting NR contributions gives rise to the time-dependent resonant CARS

signal in this limit:

$$\begin{aligned} S_{\text{CARS}}^{(3)}(\omega_s, \tau_{12} = 0, \tau_{23}) &\propto \left| \sum_{a,c} I_{ca} e^{-i\omega_{ca}\tau_{23} - \Gamma_{ca}\tau_{23}} \cdot \tilde{E}_3(\omega_s - [\omega_{ca} + \omega_3]) \right. \\ &\left. \cdot e^{(\Gamma_{ca}^2 \tau_G^2/4)} e^{i(\Gamma_{ca}[\omega_{ca} - \Delta]\tau_G^2/2)} \right|^2. \end{aligned} \quad (\text{B3})$$

From Eq. (B3), it is clear that the tr-CARS frequency-domain signal is expected to exhibit a series of peaks with Gaussian profiles that are centered at  $\omega_s = \omega_{ca} + \omega_3$  and weighted by factors that depend on transition dipoles associated with the four-pulse pathways depicted in Fig. 1 (via  $I_{ca}$ ) and the dephasing rates (via  $\Gamma_{ca}$ ). Moreover, in cases where the difference (i.e., beat) frequencies between multiple molecular transition frequencies,  $\omega_{ca,c'd} = \omega_{c'd} - \omega_{ca}$ , lie within the bandwidth of the broadband pulse 3, these Gaussian profiles will overlap and give rise to interferences that exhibit intensity oscillations as a function of the scanned timescale,  $\tau_{23}$ , by virtue of the decaying oscillatory exponential factor within each term of the summation. Upon squaring of the summation over states, these beat frequencies decay with rates,  $\Gamma_{ca,c'd} = \Gamma_{c'd} + \Gamma_{ca}$ , that are dependent on the dephasing timescales of each individual transition. Thus, while Eq. (B3) demonstrates that the outgoing signal of fs tr-CARS in principle contains all molecular information (including relative cross-sections, frequencies, and dephasing rates) associated with a spontaneous Raman spectrum of the molecular species,<sup>20,32,33</sup> two of the major deficiencies of fs tr-CARS, noted previously,<sup>1</sup> are also emphasized: (1) absolute molecular frequencies are not measured directly; only beat frequencies,  $\omega_{ca,c'd}$ , spectrally centered at the average frequency associated with the two contributing transitions [ $\frac{1}{2} \cdot (\omega_{ca} + \omega_{c'd})$ ], are observed in the oscillating intensities of the broadband CARS output spectrum [note that this is not an issue in the specific case of DFWM, where beats between vibrational or rotational states of interest and the vibrationless/rotationless (Rayleigh) transition can be observed directly]; and (2) it is difficult to deduce dephasing rates associated with individual molecular transitions directly from such measurements, since the measured decay timescale of each observed beat frequency results from the average of the dephasing rates of the two contributing transitions.<sup>24</sup>

### 2. Simulation of gas-phase fs tr-CARS experiments

Simulations of fs tr-CARS results have been carried out to emphasize the prominent features of fs tr-CARS experiments. Fig. 9 depicts the time- and frequency-resolved signal expected from a traditional fs tr-CARS measurement of  $\text{N}_2$  gas at an adiabatic flame temperature of  $T = 2370$  K. These calculations have been carried out numerically using Eqs. (1) and (5) assuming a Gaussian transform-limited fs-duration probe pulse ( $\tau_G = 65$  fs) with a corresponding Gaussian frequency-domain intensity profile (FWHM  $\sim 190$   $\text{cm}^{-1}$ ). Similar bandwidths are assumed for the time-overlapped ( $\tau_{12} = 0$ ) pulses 1 and 2. In this flame-temperature  $\text{N}_2$

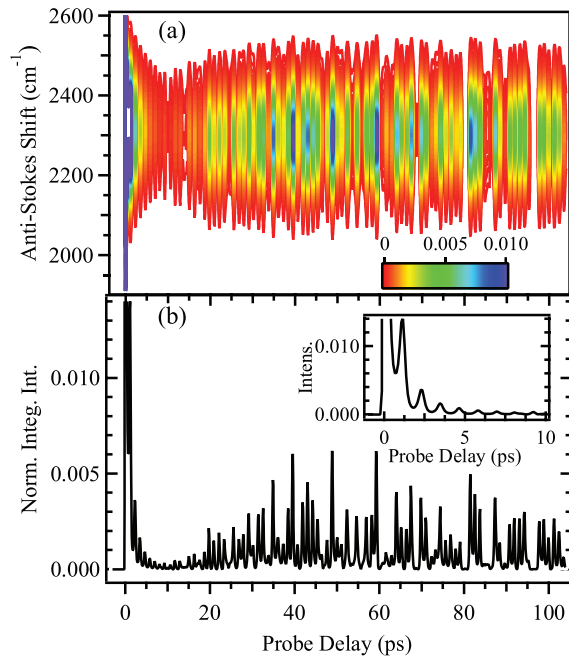


FIG. 9. Simulated fs tr-CARS signal for  $N_2$  at 2370 K. (a) Contour plot (linear color scale shown, normalized to peak intensity at zero probe delay) depicts the frequency- and time-resolved spectra as a function of probe delay; (b) spectrally integrated signal (normalized to peak intensity at zero probe delay) as a function of probe delay. Inset depicts expanded 0–10 ps region to emphasize vibrational beats.

example, over 200 contributing  $Q$ -branch molecular transition frequencies span a range of  $\sim 100 \text{ cm}^{-1}$  and are, therefore, not resolved in the frequency domain. Thus, as depicted in the contour plot shown in Fig. 9(a), the observed spectrally resolved CARS signal exhibits little spectral variance as a function of probe-pulse delay ( $\tau_{23}$ ); at a given delay, the observed signal appears as a broad Gaussian-like spectrum that results from the interference of many Gaussian profiles centered at the contributing  $Q$ -branch transition frequencies [Eq. (B3)]. Because of this high degree of molecular spectral congestion relative to the broadband probe-pulse width, nearly all of the relevant spectral information associated with  $N_2$  is instead observed in the time domain, as shown in the spectrally integrated signal [Fig. 9(b)]. This resultant highly structured time-domain signal has been explored at length, and is known to exhibit a series of partial recurrences<sup>22</sup> following an initial frequency-spread dephasing.<sup>80,81</sup> Moreover, both of these features result from the many pairs of beat frequencies associated with the interfering molecular transitions contained within the bandwidth of the probe pulse and are highly dependent on relative thermalized state populations. For example, the regularly spaced series of peaks with a 1.16-ps recurrence period observed during the 0–10 ps delay time correspond to vibrational beats associated with a series of transitions separated by  $\sim 28.7 \text{ cm}^{-1}$ , a value that corresponds to twice the vibrational anharmonicity of  $N_2$ ,<sup>22</sup> as temperature increases and the relative population of vibrationally excited  $N_2$  increases accordingly, the amplitude of this recurrence feature increases as well.<sup>81</sup>

## APPENDIX C: LONG PROBE PULSE (ps-CARS LIMIT)

### 1. Theoretical treatment of CARS with long pulse 3

To examine the frequency-dependent aspects of CARS experiments with long probe-pulse durations, the extreme limiting case of a monochromatic (cw) field 3 can be explored analytically. Although this approximation will be rigorous only in cases where the probe pulse is long compared to molecular dephasing timescales, it still provides insight into the frequency-domain signals observed in several CARS approaches using ps- or ns-duration probes. In this case, by assuming  $E_3(t) = 1$ , Eq. (7) reduces to

$$P_{\text{CARS}}^{(3)}(\Delta, \tau_{12} = 0, \tau_{23}) = \frac{1}{\sqrt{2\pi}} \left(\frac{1}{\hbar}\right)^3 e^{-i\Delta\tau_{23}} \times \sum_{a,c} I_{ca} \frac{1}{(\Delta + \omega_1 - \omega_2 - \omega_{ca}) + i\Gamma_{ca}}, \quad (\text{C1})$$

and the detected CARS signal is

$$S_{\text{CARS}}(\omega_s, \tau_{12} = 0, \tau_{23}) \propto \left| \sum_{a,c} I_{ca} \frac{1}{(\omega_s - (\omega_{ca} + \omega_3)) + i\Gamma_{ca}} \right|^2. \quad (\text{C2})$$

As expected for a cw field 3, these expressions are independent of  $\tau_{23}$ , and all spectral information arising from such a probe scheme is observed purely in the frequency-domain intensities and lineshapes. Thus, a cw field 3 (or a pulse 3 in which  $E_3(t)$  is essentially constant during the timescale of the molecular third-order response, such as is typically the case in ns-CARS experiments) is expected to give rise to CARS signal that consists of the squared magnitude of a sum of complex Lorentzian lineshapes centered at frequencies  $(\omega_{ca} + \omega_3)$  with linewidth parameters of  $\Gamma_{ca}$ . In the case of isolated frequencies (i.e., the separation between transitions is large relative to their dephasing rates), the observed spectrum will consist of isolated peaks proportional to

$$\left| \frac{1}{(\omega_s - (\omega_{ca} + \omega_3)) + i\Gamma_{ca}} \right|^2 = \frac{1}{[\omega_s - (\omega_{ca} + \omega_3)]^2 - (\Gamma_{ca})^2}, \quad (\text{C3})$$

which are simply Lorentzian lineshapes centered at frequencies,  $\omega_s = (\omega_{ca} + \omega_3)$  (i.e., the anti-Stokes shifted frequency relative to the probe-pulse frequency,  $\omega_3$ ), with linewidths (FWHM) of  $2 \cdot \Gamma_{ca}$ . In this well-separated limit, then, a long-pulse-3 probe scheme is expected to provide spectra with linewidths identical to those of the spontaneous Raman spectrum, arising from the fact that the squared magnitude of a complex Lorentzian is proportional to its imaginary component (i.e.,  $|L(\omega)|^2 \propto \text{Im}\{L(\omega)\}$ ). In cases where the linewidths of the molecular transitions are comparable to or larger than the spacing between these transitions, however, Eq. (C2) demonstrates that interferences will be observed between spectrally overlapping peaks. Moreover, in this limiting long-probe-pulse example, the presence of a strong NR contribution necessarily results in interference between the resonant spectrum and the corresponding broadband NR contributions

that result from the insertion of  $\Gamma_{NR}$  (which is large compared to all molecular dephasing rate constants,  $\Gamma_{ca}$ ) into one term in Eq. (C2).

## 2. Simulation of gas-phase ps-CARS experiments

As noted above, this long-pulse-3 limiting case is representative of cases in which the probe-pulse duration is long compared to the molecular decay timescales, such as is the case in traditional ns-CARS diagnostic measurements.<sup>50</sup> Under these conditions, the steady-state frequency-domain spectrum resulting from Eqs. (1) and (5) is analogous to that calculated using the Sandia CARSFT code.<sup>82</sup> Although not rigorously accurate, the infinitely long-pulse-limit analytical approximation shown in Eq. (C2) can also be used to understand the signal observed with many ps-CARS measurements, in which the ps-duration probe pulse is often comparable to or longer than the dephasing lifetimes of the molecular species. Simulated ps-CARS signals for  $N_2$  vibrational CARS at  $T = 2370$  are shown in Fig. 10, again by numerically calculating Eqs. (1) and (5). As above, broadband, fs-duration pulses 1 and 2 are assumed with corresponding bandwidths ( $\sim 200$   $cm^{-1}$ ) that are large compared to the energy range spanned by the contributing molecular transition frequencies. To match experimental conditions associated with published  $N_2$  ps-CARS results,<sup>83</sup> the probe pulse is assumed to be a Gaussian transform-limited pulse with a FWHM duration of 135 ps, and the calculated CARS signal is further convolved with a Gaussian (FWHM = 0.5  $cm^{-1}$ ) spectral response function. These results, which match the qualitative features observed in this previous experimental work,<sup>83</sup> emphasize the features associated with the long-pulse-3 limit; in particular, the many contributing transitions exhibit high spectral resolution at both a probe-pulse delay of 0 ps and 165 ps. A comparison of these two signals, however, emphasizes the small degree of temporal dependence observed in this ps-CARS signal that cannot be predicted by the long-pulse-3 limit assumption of a cw probe pulse. In particular, the  $\tau_{23} = 0$  spectrum contains considerable NR contributions that are absent in the signal at  $\tau_{23} = 165$  ps. Moreover, the use of a time-delayed probe pulse has a slight line-narrowing effect, discussed in greater detail in Sec. IV A in addressing the top-hat probe pulse shape. This effect is most notable, both in experimental results<sup>83</sup> and in the simulations shown in Fig. 10, at the high-frequency bandhead (near 2330  $cm^{-1}$ ) of

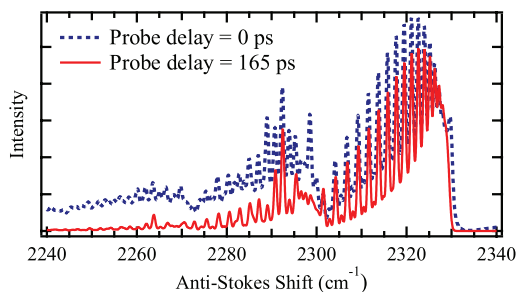


FIG. 10. Simulated ps-CARS signal from  $N_2$  at 2370 K, assuming fs-duration broadband pulses 1 and 2 and a 135-ps-duration probe pulse; signal depicted at probe delays ( $\tau_{23}$ ) of 0 ps (dashed curve) and 165 ps (solid curve).

the vibrational CARS signal, where the delayed-probe ( $\tau_{23} = 165$  ps) spectrum exhibits a slightly sharper high-frequency cutoff than is observed in the  $\tau_{23} = 0$  data.<sup>83</sup>

- <sup>1</sup>B. D. Prince, A. Chakraborty, B. M. Prince, and H. U. Stauffer, *J. Chem. Phys.* **125**, 044502 (2006).
- <sup>2</sup>B. D. Prince, A. Chakraborty, B. M. Prince, and H. U. Stauffer, in *Femtochemistry VII: Fundamental Ultrafast Processes in Chemistry, Physics, and Biology*, edited by A. W. Castleman, Jr. and M. L. Kimble (Elsevier, Amsterdam, 2006), p. 70.
- <sup>3</sup>D. Pestov, R. K. Murawski, G. O. Ariunbold, X. Wang, M. C. Zhi, A. V. Sokolov, V. A. Sautenkov, Y. V. Rostovtsev, A. Dogariu, Y. Huang, and M. O. Scully, *Science* **316**, 265 (2007).
- <sup>4</sup>D. Pestov, X. Wang, G. O. Ariunbold, R. K. Murawski, V. A. Sautenkov, A. Dogariu, A. V. Sokolov, and M. O. Scully, *Proc. Natl. Acad. Sci. U.S.A.* **105**, 422 (2008).
- <sup>5</sup>J. D. Miller, M. N. Slipchenko, T. R. Meyer, H. U. Stauffer, and J. R. Gord, *Opt. Lett.* **35**, 2430 (2010).
- <sup>6</sup>J. D. Miller, M. N. Slipchenko, and T. R. Meyer, *Opt. Express* **19**, 13326 (2011).
- <sup>7</sup>J. D. Miller, S. Roy, M. N. Slipchenko, J. R. Gord, and T. R. Meyer, *Opt. Express* **19**, 15627 (2011).
- <sup>8</sup>J. D. Miller, S. Roy, J. R. Gord, and T. R. Meyer, *J. Chem. Phys.* **135**, 201104 (2011).
- <sup>9</sup>J. D. Miller, C. E. Dedic, S. Roy, J. R. Gord, and T. R. Meyer, *Opt. Express* **20**, 5003 (2012).
- <sup>10</sup>H. U. Stauffer, J. D. Miller, S. Roy, J. R. Gord, and T. R. Meyer, *J. Chem. Phys.* **136**, 111101 (2012).
- <sup>11</sup>S. P. Kearney and D. J. Scoglietti, *Opt. Lett.* **38**, 833 (2013).
- <sup>12</sup>S. P. Kearney, D. J. Scoglietti, and C. J. Kliever, *Opt. Express* **21**, 12327 (2013).
- <sup>13</sup>R. Leonhardt, W. Holzappel, W. Zinth, and W. Kaiser, *Rev. Phys. Appl. (Paris)* **22**, 1735 (1987).
- <sup>14</sup>R. Inaba, H. Okamoto, K. Yoshihara, and M. Tasumi, *Chem. Phys. Lett.* **185**, 56 (1991).
- <sup>15</sup>T. Joo and A. C. Albrecht, *J. Chem. Phys.* **99**, 3244 (1993).
- <sup>16</sup>M. Morgen, W. Price, L. Hunziker, P. Ludowise, M. Blackwell, and Y. Chen, *Chem. Phys. Lett.* **209**, 1 (1993).
- <sup>17</sup>C. C. Hayden and D. W. Chandler, *J. Chem. Phys.* **103**, 10465 (1995).
- <sup>18</sup>M. Schmitt, G. Knopp, A. Materny, and W. Kiefer, *J. Phys. Chem. A* **102**, 4059 (1998).
- <sup>19</sup>T. Lang, K. L. Kompa, and M. Motzkus, *Chem. Phys. Lett.* **310**, 65 (1999).
- <sup>20</sup>M. Heid, S. Schlücker, U. Schmitt, T. Chen, R. Schweitzer-Stenner, V. Engel, and W. Kiefer, *J. Raman Spectrosc.* **32**, 771 (2001).
- <sup>21</sup>T. Lang, M. Motzkus, H. M. Frey, and P. Beaud, *J. Chem. Phys.* **115**, 5418 (2001).
- <sup>22</sup>P. Beaud, H. M. Frey, T. Lang, and M. Motzkus, *Chem. Phys. Lett.* **344**, 407 (2001).
- <sup>23</sup>G. Knopp, P. Beaud, P. Radi, M. Tulej, B. Bougie, D. Cannavo, and T. Gerber, *J. Raman Spectrosc.* **33**, 861 (2002).
- <sup>24</sup>S. Schlücker, M. Heid, R. K. Singh, B. P. Asthana, J. Popp, and W. Kiefer, *Z. Phys. Chem.* **216**, 267 (2002).
- <sup>25</sup>G. Knopp, P. Radi, M. Tulej, T. Gerber, and P. Beaud, *J. Chem. Phys.* **118**, 8223 (2003).
- <sup>26</sup>S. Roy, J. R. Gord, and A. K. Patnaik, *Prog. Energy Combust. Sci.* **36**, 280 (2010).
- <sup>27</sup>F. El-Diasty, *Vib. Spectrosc.* **55**, 1 (2011).
- <sup>28</sup>S. R. Engel, J. D. Miller, C. E. Dedic, T. Seeger, A. Leipertz, and T. R. Meyer, *J. Raman Spectrosc.* **44**, 1336 (2013).
- <sup>29</sup>M. N. Slipchenko, B. D. Prince, S. C. Ducatman, and H. U. Stauffer, *J. Phys. Chem. A* **113**, 135 (2009).
- <sup>30</sup>A. Bohlin, B. D. Patterson, and C. J. Kliever, *J. Chem. Phys.* **138**, 081102 (2013).
- <sup>31</sup>A. Bohlin and C. J. Kliever, *J. Chem. Phys.* **138**, 221101 (2013).
- <sup>32</sup>D. C. Urbanek and M. A. Berg, *J. Chem. Phys.* **127**, 044306 (2007).
- <sup>33</sup>S. Nath, D. C. Urbanek, S. J. Kern, and M. A. Berg, *J. Chem. Phys.* **127**, 044307 (2007).
- <sup>34</sup>J. R. Gord, T. R. Meyer, and S. Roy, *Annu. Rev. Anal. Chem.* **1**, 663 (2008).
- <sup>35</sup>L. Ujj, B. L. Volodin, A. Popp, J. K. Delaney, and G. H. Atkinson, *Chem. Phys.* **182**, 291 (1994).
- <sup>36</sup>S. Takeuchi and T. Tahara, *Chem. Phys. Lett.* **326**, 430 (2000).
- <sup>37</sup>T. Siebert, M. Schmitt, V. Engel, A. Materny, and W. Kiefer, *J. Am. Chem. Soc.* **124**, 6242 (2002).

- <sup>38</sup>T. Siebert, R. Maksimenka, A. Materny, V. Engel, W. Kiefer, and M. Schmitt, *J. Raman Spectrosc.* **33**, 844 (2002).
- <sup>39</sup>S. Fujiyoshi, S. Takeuchi, and T. Tahara, *J. Phys. Chem. A* **107**, 494 (2003).
- <sup>40</sup>T. Siebert, V. Engel, A. Materny, W. Kiefer, and M. Schmitt, *J. Phys. Chem. A* **107**, 8355 (2003).
- <sup>41</sup>D. F. Underwood and D. A. Blank, *J. Phys. Chem. A* **107**, 956 (2003).
- <sup>42</sup>S. Fujiyoshi, T. Ishibashi, and H. Onishi, *J. Phys. Chem. A* **108**, 11165 (2004).
- <sup>43</sup>S. Fujiyoshi, S. Takeuchi, and T. Tahara, *J. Phys. Chem. A* **108**, 5938 (2004).
- <sup>44</sup>T. Hornung, H. Skenderović, and M. Motzkus, *Chem. Phys. Lett.* **402**, 283 (2005).
- <sup>45</sup>R. Maksimenka, B. Dietzek, A. Szeghalmi, T. Siebert, W. Kiefer, and M. Schmitt, *Chem. Phys. Lett.* **408**, 37 (2005).
- <sup>46</sup>J. Hauer, T. Backup, and M. Motzkus, *J. Phys. Chem. A* **111**, 10517 (2007).
- <sup>47</sup>B. D. Prince, A. Chakraborty, B. M. Prince, T.-M. Hsin, and H. U. Stauffer, in *Femtochemistry VII: Fundamental Ultrafast Processes in Chemistry, Physics, and Biology*, edited by A. W. Castleman, Jr. and M. L. Kimble (Elsevier, Amsterdam, 2006), p. 66.
- <sup>48</sup>J. P. Ogilvie, M. Cui, D. Pestov, A. V. Sokolov, and M. O. Scully, *Mol. Phys.* **106**, 587 (2008).
- <sup>49</sup>A. M. Weiner, *Rev. Sci. Instrum.* **71**, 1929 (2000).
- <sup>50</sup>R. D. Hancock, K. E. Bertagnolli, and R. P. Lucht, *Combust. Flame* **109**, 323 (1997).
- <sup>51</sup>S. Mukamel, *Principles of Nonlinear Optical Spectroscopy* (Oxford University Press, New York, 1995).
- <sup>52</sup>F. M. Kanga and M. G. Sceats, *Opt. Lett.* **5**, 126 (1980).
- <sup>53</sup>P. J. Wrzesinski, H. U. Stauffer, W. D. Kulatilaka, J. R. Gord, and S. Roy, *J. Raman Spectrosc.* **44**, 1344 (2013).
- <sup>54</sup>P. W. Dooley, I. V. Litvinyuk, K. F. Lee, D. M. Rayner, M. Spanner, D. M. Villeneuve, and P. B. Corkum, *Phys. Rev. A* **68**, 023406 (2003).
- <sup>55</sup>S. Roy, P. S. Hsu, N. Jiang, J. R. Gord, W. D. Kulatilaka, H. U. Stauffer, and J. R. Gord, *J. Chem. Phys.* **138**, 024201 (2013).
- <sup>56</sup>A. Lagutchev, S. A. Hambir, and D. D. Dlott, *J. Phys. Chem. C* **111**, 13645 (2007).
- <sup>57</sup>A. Lagutchev, A. Lozano, P. Mukherjee, S. A. Hambir, and D. D. Dlott, *Spectrochim. Acta Pt. A* **75**, 1289 (2010).
- <sup>58</sup>S. O. Konorov, M. W. Blades, and R. F. B. Turner, *Appl. Spectrosc.* **64**, 767 (2010).
- <sup>59</sup>W. D. Kulatilaka, P. S. Hsu, H. U. Stauffer, J. R. Gord, and S. Roy, *Appl. Phys. Lett.* **97**, 081112 (2010).
- <sup>60</sup>H. U. Stauffer, W. D. Kulatilaka, P. S. Hsu, J. R. Gord, and S. Roy, *Appl. Opt.* **50**, A38 (2011).
- <sup>61</sup>W. D. Kulatilaka, H. U. Stauffer, J. R. Gord, and S. Roy, *Opt. Lett.* **36**, 4182 (2011).
- <sup>62</sup>S. Roy, W. D. Kulatilaka, D. R. Richardson, R. P. Lucht, and J. R. Gord, *Opt. Lett.* **34**, 3857 (2009).
- <sup>63</sup>D. R. Richardson, R. P. Lucht, W. D. Kulatilaka, S. Roy, and J. R. Gord, *Appl. Phys. B* **104**, 699 (2011).
- <sup>64</sup>D. R. Richardson, R. P. Lucht, W. D. Kulatilaka, S. Roy, and J. R. Gord, *J. Opt. Soc. Am. B* **30**, 188 (2013).
- <sup>65</sup>M. L. Orlov, J. F. Ogilvie, and J. W. Nibler, *J. Mol. Spectrosc.* **185**, 128 (1997).
- <sup>66</sup>M. A. Buldakov, V. N. Cherepanov, B. V. Korolev, and I. I. Matrosov, *J. Mol. Spectrosc.* **217**, 1 (2003).
- <sup>67</sup>M. Marrocco, *J. Raman Spectrosc.* **40**, 741 (2009).
- <sup>68</sup>L. A. Rahn and R. E. Palmer, *J. Opt. Soc. Am. B* **3**, 1164 (1986).
- <sup>69</sup>L. Martinsson, P. E. Bengtsson, M. Alden, S. Kröll, and J. Bonamy, *J. Chem. Phys.* **99**, 2466 (1993).
- <sup>70</sup>C. J. Kliewer, A. Bohlin, E. Nordstrom, B. D. Patterson, P. E. Bengtsson, and T. B. Settersten, *Appl. Phys. B* **108**, 419 (2012).
- <sup>71</sup>L. A. Rahn, R. L. Farrow, and G. J. Rosasco, *Phys. Rev. A* **43**, 6075 (1991).
- <sup>72</sup>G. Millot, R. Saint-Loup, J. Santos, R. Chauv, H. Berger, and J. Bonamy, *J. Chem. Phys.* **96**, 961 (1992).
- <sup>73</sup>T. Seeger, F. Beyrau, A. Bräuer, and A. Leipertz, *J. Raman Spectrosc.* **34**, 932 (2003).
- <sup>74</sup>A. Roblin, J. Bonamy, D. Robert, M. Lefebvre, and M. Pealat, *J. Phys. II France* **2**, 285 (1992).
- <sup>75</sup>M. L. Koszykowski, L. A. Rahn, R. E. Palmer, and M. E. Coltrin, *J. Phys. Chem.* **91**, 41 (1987).
- <sup>76</sup>M. L. Koszykowski, R. L. Farrow, and R. E. Palmer, *Opt. Lett.* **10**, 478 (1985).
- <sup>77</sup>F. Beyrau, A. Datta, T. Seeger, and A. Leipertz, *J. Raman Spectrosc.* **33**, 919 (2002).
- <sup>78</sup>R. L. Farrow, R. Trebino, and R. E. Palmer, *Appl. Opt.* **26**, 331 (1987).
- <sup>79</sup>N. Dudovich, D. Oron, and Y. Silberberg, *J. Chem. Phys.* **118**, 9208 (2003).
- <sup>80</sup>R. P. Lucht, S. Roy, T. R. Meyer, and J. R. Gord, *Appl. Phys. Lett.* **89**, 251112 (2006).
- <sup>81</sup>S. Roy, P. J. Kinnius, R. P. Lucht, and J. R. Gord, *Opt. Commun.* **281**, 319 (2008).
- <sup>82</sup>R. E. Palmer, SAND89-8206, 1989.
- <sup>83</sup>T. R. Meyer, S. Roy, and J. R. Gord, *Appl. Spectrosc.* **61**, 1135 (2007).